

1 **Limestone calcination nearby equilibrium: Kinetics, CaO crystal**
2 **structure, sintering and reactivity**

3 J. M. Valverde^a, P. E. Sanchez-Jimenez^b, L. A. Perez-Maqueda^b

4 ^a Faculty of Physics. University of Seville. Avenida Reina Mercedes s/n, 41012 Sevilla, Spain

5 ^b Instituto de Ciencia de Materiales de Sevilla (C.S.I.C.-Univ.

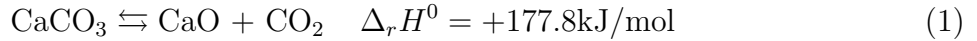
6 Seville), Americo Vespucio 49, 41092 Sevilla, Spain

Abstract

In this work we analyze limestone calcination at environmental conditions involving a CO_2 partial pressure P close to the equilibrium pressure P_{eq} by means of in-situ X-ray diffraction (XRD) and thermogravimetric (TG) analyses. In contrast with previous empirical observations carried out mostly at conditions far from equilibrium ($P/P_{eq} \ll 1$), our results show that the decarbonation rate decreases as the temperature is increased while P/P_{eq} is kept constant, which is explained from a reaction mechanism including desorption and the exothermic structural transformation from metastable CaO^* nanocrystals to the stable CaO form. The crystal structure and sintering of nascent CaO during calcination has been investigated from in-situ XRD analysis, physisorption analysis and Scanning Electron Microscopy (SEM), which shows that the ratio of the size of polycrystalline CaO grains to crystallite size increases linearly with the CO_2 partial pressure in the calcination atmosphere. For high CO_2 partial pressures, the size of CaO grains reaches a maximum value of around $1 \mu\text{m}$, which leads to a residual surface area of about $1 \text{ m}^2/\text{g}$, whereas in the limit $P \rightarrow 0$ grain size and crystallite size (of the order of 10 nm) would coincide. Accordingly, sintering in the presence of CO_2 would be triggered by the agglomeration of CaO crystals enhanced by CO_2 adsorption, which increases the surface energy. The carbonation reactivity of CaO resulting from calcination scales proportionally to its surface area and is not determined by a growth of the CaO exposed surface along a preferred crystallographic direction wherein carbonation would be unfavorable as suggested in recent works.

27 I. INTRODUCTION

28 The endothermic decomposition of limestone (CaCO_3)



29 is at the heart of a myriad of industrial and natural processes (see [1] and references therein).
30 Lime (CaO) is a main ingredient of technologies employed in a wide variety of industries
31 such as construction, agriculture, food processing, disinfection, water treatment, SO_2 post-
32 combustion capture, steel-making, plastics and glass, and sugar refining. Nowadays, the
33 number of applications wherein this apparently simple decomposition reaction plays a cen-
34 tral role continues to add on. The Ca-looping (CaL) technology, which is built on the
35 multicyclic calcination/carbonation of limestone, has recently emerged as a feasible process
36 for CO_2 capture from industrial concentrated sources such as coal combustion plants [2–4].
37 The CaL technology is being currently investigated as a method to store and controllably
38 dispatch thermal energy in concentrated solar power plants (CSP) [5] as early proposed in
39 the 1980s [6]. The wide availability, low cost and harmlessness towards the environment of
40 natural limestone would contribute to boost the competitiveness of these processes to reach
41 a commercial level. Nevertheless, a number of issues might still hamper their large scale
42 development such as the marked deceleration of decomposition when calcination is carried
43 out under high CO_2 partial pressure and high temperature as required in post-combustion
44 CO_2 capture and the poor carbonation reactivity of CaO resulting from decomposition at
45 these conditions [7, 8]. Certainly, a fundamental understanding of the physic-chemical pro-
46 cesses that govern the thermal decomposition of CaCO_3 would be of paramount importance
47 in order to devise strategies for improving the efficiency of technical applications in which

48 this reaction is involved.

49 A vast number of studies may be found in the literature with the goal of getting a grip on
50 the driving mechanisms behind the CaCO_3 thermal decomposition [1, 9–19]. Most of them
51 analyze the reaction kinetics as affected by the calcination temperature T and the CaCO_3
52 conversion degree α (ratio of mass of CaCO_3 decarbonated to initial mass). The conversion
53 rate is commonly measured by means of thermogravimetric analysis (TGA) and can be in
54 general well fitted by the widely accepted Arrhenius type law

$$\frac{d\alpha}{dt} = A f(\alpha) \exp(-E/RT) \left(1 - \frac{P}{P_{eq}}\right)^\gamma \quad (2)$$

55 where A is a pre-exponential term, $\gamma \sim 1$, $E > 0$ is the so-called activation energy, $R =$
56 8.3145 J/mol-K is the ideal gas constant, P is the CO_2 partial pressure and P_{eq} is the CO_2
57 partial pressure for the reaction to be at equilibrium, which is given by

$$P_{eq}(\text{atm}) \approx 4.083 \times 10^7 \exp(-20474/T) \quad (3)$$

58 as inferred from thermochemical empirical data [17, 20, 21]. Even though Eq. 2 is widely
59 accepted, the Arrhenius equation for solid-state reactions is hardly justifiable from purely
60 theoretical grounds since the Maxwell–Boltzmann equation on which it is based is only
61 applicable to the energy distribution of molecules in an ideal gas and not to the immobilized
62 ions of a crystalline reactant [19, 22]. Moreover, the decarbonation process generally consists
63 of several steps such as chemical decomposition, structural transformation and physical
64 desorption.

65 A number of functional forms $f(\alpha)$ have been proposed to account for the influence on
66 the reaction progress of diverse mechanisms such as nucleation and growth, impeded CO_2
67 diffusion or geometrical constraints related to particles' shape and pore size distribution of

68 the powder [23], whose relative importance generally depends on the particular conditions
69 of calcination [16]. In regards to the pressure term in the right hand side of Eq. 2, it is
70 often neglected since experimental conditions usually imply $P \ll P_{eq}$ [1, 9, 11–13, 15–
71 17, 19, 24]. Under these conditions, chemical decomposition is supposed to be the only
72 relevant step of the reaction and the conversion rate is generally well fitted in a broad range
73 of conversion by the product of the mechanistic-rate function $f(\alpha)$ and an Arrhenius law
74 with apparent activation energies around the reaction enthalpy change, mainly between
75 100 and 230 kJ/mol [22]. However, the widely spread range of activation energies found
76 experimentally, which is also observed for decomposition of single calcite crystals [1, 24],
77 suggests that the reaction rate is not exclusively determined by chemical decomposition [19,
78 24]. The apparent activation energy in Eq. 2 should be interpreted in terms of the activation
79 energies and enthalpy variations of the preponderant mechanisms which may in turn be a
80 function of the degree of conversion α [19]. On the other hand, experimental evidences
81 indicate [1, 24] that decomposition of calcite yields a metastable solid phase product whose
82 transformation into the stable CaO is exothermic [18, 25] although it is seen to occur very
83 fast in the limit $P/P_{eq} \ll 1$ to have any possible influence on the reaction rate [1].

84 In the study on limestone decomposition reported in the present manuscript, the ap-
85 proach adopted was motivated by the calcination conditions in the recently emerged Ca-
86 looping technology for post-combustion CO₂ capture. In this novel application, the CO₂
87 sorbent (CaO) has to be regenerated in a fluidized bed reactor (calciner) operated at atmo-
88 spheric pressure and where the partial pressure of CO₂ must be necessarily high (between
89 70 and 90 kPa) in order to retrieve from it a stream of CO₂ at high concentration to be
90 compressed, transported and stored. Therefore, calcination temperatures have to be rather
91 high (typically above 900°C) in order to shift the reaction equilibrium towards decarbon-

102 ation. Moreover, full decarbonation has to be achieved in typically short residence times
103 (on the order of minutes) due to technological constraints, which demands increasing even
104 further the calcination temperature to values close to 950°C. This imposes an important
105 energy penalty and hinders the industrial competitiveness of the technology [26–29]. A fur-
106 ther issue is that the CaO stemming from calcination at high CO₂ partial pressure and high
107 temperature has a significantly low carbonation reactivity [7, 8]. Diverse strategies have
108 been devised aimed at decreasing the calcination temperature such as using low crystalline
109 limestone or dolomite, which exhibit a faster decomposition at high CO₂ partial pressure
110 [8, 30].

111 In our work, we have investigated limestone decarbonation at CO₂ partial pressure and
112 temperature conditions nearby equilibrium ($P/P_{eq} \lesssim 1$). To this end calcination tests have
113 been carried out in a broad range of temperatures and for CO₂ partial pressures close
114 to the equilibrium pressure. TGA tests were complemented with in-situ X-ray diffraction
115 (XRD) analysis allowing us to investigate the time evolution of CaO crystal structure during
116 decarbonation. A further subject that has been studied is the sintering and carbonation
117 reactivity of CaO derived from calcination at conditions nearby equilibrium. In-situ XRD
118 and SEM analyses served to look at the quantitative correlation between the reduction of
119 surface area due to sintering and CaO reactivity as determined by the calcination conditions.
120 The in-situ XRD analysis helped us extracting information also on the linkage between the
121 transformation mechanism, CaO crystal size enlargement and sintering. Moreover, it allowed
122 us investigating whether the very low reactivity of CaO resulting from calcination at high
123 temperature and high CO₂ pressure might be caused by a preferential orientation of the CaO
124 surface along poorly reactive (200) crystallographic planes (on which CO₂ chemisorption is
125 energetically unfavorable at high temperature [31–33]) and not merely due to the reduction

116 of CaO surface area by sintering.

117 II. MATERIALS AND METHODS

118 The limestone tested in our work has been a natural limestone from Matagallar quarry
119 (Pedrera, Spain) of high purity (99.62% CaCO₃, SiO₂ < 0.05%, Al₂O₃ < 0.05%, 0.24%
120 MgO, 0.08% Na₂O) and a small particle size (9.5 μm volume weighted mean particle size)

121 X-ray diffraction (XRD) analysis was performed using a Bruker D8 Advance powder
122 diffractometer equipped with a high temperature chamber (Anton Paar XRK 900) and a fast
123 response/high sensitivity detector (Bruker Vantec 1) allowing us to look at the time evolution
124 of the crystal structure in-situ as calcination progresses. A sufficiently large number of
125 counts is retrieved by means of 140 s duration XRD scans continuously recorded in the
126 range $2\theta \in (27.5^\circ, 39.5^\circ)$ (0.022°/step) wherein the main Bragg reflection peaks for calcite
127 and lime are located. Since the interaction volume of the Cu K-alpha radiation (0.15405 nm
128 wavelength) employed in the equipment with the sample typically comprises a depth of up
129 to 100 μm, which is much larger than particle size, the diffractograms obtained are useful to
130 reliably estimate the CaCO₃/CaO weight fraction during in-situ calcination by means of a
131 semi-quantitative analysis. In this setup, the limestone sample is held on a 1 cm diameter
132 porous ceramic plate through which a N₂/CO₂ mixture (with controlled CO₂ vol.%) is passed
133 at a small flow rate (100 cm³min⁻¹) and atmospheric pressure. The temperature is increased
134 from ambient temperature at 12°C/min up to the target calcination temperature, which is
135 kept constant for about 1 h while XRD scans are continuously registered.

136 The kinetics of limestone decomposition was also investigated in our work by means of
137 TGA at the same conditions as those employed in the XRD analysis. TGA tests were carried
138 out using a Q5000IR TG analyzer (TA Instruments). This instrument is provided with an

139 infrared furnace heated by halogen lamps and a high sensitivity balance ($<0.1 \mu\text{g}$) charac-
140 terized by a minimum baseline dynamic drift ($<10 \mu\text{g}$). TGA was also employed to measure
141 the carbonation reactivity of CaO resulting from calcination, which was accomplished by
142 quickly decreasing the temperature down to 650°C ($300^\circ\text{C}/\text{min}$ rate) and subjecting the
143 sample to a gas mixture of 85% dry air/15% CO_2 vol/vol (typical of post-combustion flue
144 gas) for 5 min.

145 In order to obtain reliable kinetic data from both XRD and TGA tests it is of great im-
146 portance to minimize mass and heat transfer phenomena that might influence the reaction
147 rate uncontrollably. As noted in previous works on the kinetics of limestone decomposition
148 based on TGA, undesired effects due to diffusion resistance through the sample become rele-
149 vant in this type of analysis for sample masses above $\sim 40 \text{ mg}$ [16]. Mass transfer phenomena
150 can be neglected for sample masses of 10 mg as used in our tests. On the other hand, in-situ
151 XRD calcination tests require the use of sample masses of around 150 mg. However, the
152 gas-solid contacting efficiency in this setup is favored and mass transfer phenomena mini-
153 mized since the gas is passed directly through the sample layer whereas in the TG analyzer
154 the gas flows over it. The XRK 900 reactor chamber employed in our in-situ XRD tests is
155 specifically designed for the kinetic analysis of gas-solid reactions up to 900°C . The entire
156 set of sample and sample holder is placed inside a furnace with a heater that guarantees
157 temperature uniformity and the absence of temperature gradients in the sample. NiCr/NiAl
158 thermocouples are positioned inside the furnace and on the ceramic sample holder providing
159 a reliable measurement and control of the sample temperature. As regards the TG analyzer,
160 heat transfer phenomena are minimizing by positioning the sample inside a SiC enclosure
161 that is heated with four symmetrically placed IR lamps ensuring consistent and uniform
162 heating. Moreover, active water-cooling of the surrounding furnace body provides an ef-

163 ficient heat-sink and facilitates precise temperature and rate control. The temperature is
164 registered by a thermocouple positioned close to the sample underneath it. Quick heating
165 of the gas up to the desired temperature is achieved by using a small gas flow rate in both
166 experiments ($100 \text{ cm}^3\text{min}^{-1}$). At this small flow rate the gas velocity has no influence on the
167 reaction rate [34]. In both setups the sample chamber is specially designed without any dead
168 volumes to ensure homogeneous filling with the reaction gas. Finally, concerning particle
169 size intra-particle diffusion resistance may play a role on the reaction rate for particles of
170 size larger than $300 \mu\text{m}$ [17, 35], which is much larger than the average size of the particles
171 in our samples.

172 Scanning Electron Microscopy (SEM) analysis was made by means of a HITACHI Ultra
173 High-Resolution S-5200 on the calcined samples in the XRD tests, which were also subjected
174 to physisorption analysis using a TriStar II 3020 V1.03 analyzer operated by N_2 sorption at 77
175 K. Additional physisorption analysis was carried out using Kr at 77 K as adsorbate whose
176 small vapor pressure allows measuring very small adsorptions with reasonable precision,
177 which resulted more convenient for CaO samples with quite low specific surfaces derived
178 from calcination at severe conditions (high temperature and high CO_2 vol%).

179 Values of CO_2 partial pressure (P (kPa) \simeq CO_2 vol.% at atmospheric pressure) and
180 temperature T for which limestone decarbonation has been investigated in our tests are
181 plotted in Fig. 1 along with the equilibrium CO_2 partial pressure P_{eq} vs. T curve (Eq. 3).
182 Values of P/P_{eq} (between 0.6 and 0.85) are shown in the inset as a function of calcination
183 temperature indicating whether decarbonation was complete, partial or not even initiated
184 in the 60 min calcination period of the in-situ XRD tests. A first remarkable observation
185 is that, for a given value of P/P_{eq} , there is an important effect of temperature on the rate
186 of decarbonation in the opposed sense indicated by Eq. 2. For example, for $P/P_{eq} \simeq 0.85$,

187 decarbonation is completed in just about 20 min at 790°C (15% CO₂) whereas it is not
188 finished in the 60 min calcination period at 860°C (50% CO₂) and at 880°C (70% CO₂)
189 decarbonation is not even started. Thus, if P/P_{eq} is kept constant, decarbonation is hindered
190 as the temperature is increased.

191 III. IN-SITU XRD ANALYSIS

192 Figure 2 shows an example of the diffractograms continuously retrieved during an in-situ
193 XRD calcination test. Since each scan takes only 140 s, which is much smaller than the
194 typical decarbonation time, the analysis of these diffractograms allows us carrying out an
195 study on the reaction kinetics and the accompanying structural change. The ratio between
196 intensities of Bragg main reflection peaks for CaCO₃ (I_{211}) and CaO (I_{200}) is plotted in
197 Fig. 5 as a function of the calcination time. As already pointed out, a main feature of
198 the results is that, for similar values of P/P_{eq} , the reaction becomes substantially slower as
199 the temperature is increased. A remarkable behavior is seen for calcination at 890°C under
200 70%CO₂ ($P/P_{eq}=0.76$). Under these conditions, the CaCO₃ peak intensity remains around
201 its highest value for a long induction period of about 30 min at the calcination temperature
202 after which it starts to decrease very slowly. Calcination at 860°/50% CO₂ shows also a
203 noticeable induction period, although shorter, after the calcination temperature is reached.
204 In general, it is seen that decarbonation starts sooner and becomes quicker as the CO₂ vol.%
205 and temperature are decreased while P/P_{eq} is kept constant.

206 Taking into account the corundum numbers for calcite ($k_c = I'_{211}/I_{cor}=3.48$ for a 50:50
207 wt.% mixture of calcite with corundum) and lime ($k_l = I'_{200}/I_{cor}=4.85$ for a 50:50 wt.%
208 mixture of lime with corundum), the reference intensity ratio method usually employed
209 in XRD analysis may be used to estimate the time evolution of the CaCO₃/CaO weight

210 fraction from the measured Bragg peaks intensities ($m_{CaCO_3}/m_{CaO} \approx (k_i/k_c)I_{211}/I_{200} =$
211 $1.39I_{211}/I_{200}$). As observed in Fig. 5, the ratio I_{211}/I_{200} fits satisfactorily to an expo-
212 nential decay with time once decarbonation is initiated. Thus, $CaCO_3$ conversion (α de-
213 fined as the ratio of mass $CaCO_3$ decarbonated to initial mass) is given by $(1 - \alpha)/\alpha =$
214 $1.39 (M_{CaCO_3}/M_{CaO})(I_{211}/I_{200}) \propto \exp(-\beta t)$, where $M_{CaCO_3}/M_{CaO} = 100/56$ is the ratio of
215 molecular weights and t is time. Taking the time derivative it is readily obtained

$$\frac{d\alpha}{dt} = f(\alpha)\beta(T, P) \quad (4)$$

216 where $f(\alpha) = \alpha(1 - \alpha)$, which is consistent with the Prout-Tompkins mechanistic rate-
217 equation. Accordingly, decarbonation would be initiated after an induction period at nucle-
218 ation sites with enhanced local reactivity such as surface structural defects. The reaction
219 would be then auto-catalyzed and accelerated as decarbonation progresses finishing with
220 a deceleration period [23, 36]. The existence of an induction period for decarbonation of
221 calcite crystals to be started in CO_2 enriched atmospheres was already observed by Hyatt
222 et al. [9].

223 Assuming that the reaction is initiated at specific reactive sites near the crystal's struc-
224 tural imperfections, an increase of the density of defects and dislocations by pretreatment
225 would serve to enhance nucleation. Results reported elsewhere [8] showing that pretreat-
226 ment by ball milling enhances decarbonation at high temperature nearby equilibrium are
227 consistent with this picture.

228 Equation 4 indicates that the dependence of the reaction rate (for a given value of conver-
229 sion α) on CO_2 partial pressure P and temperature T at the conditions close to equilibrium
230 of our experiments may be expressed separately by the function $\beta(T, P)$, which does not
231 conform to the widely accepted Arrhenius law with a positive activation energy (Eq. 2).

232 Contrarily, we see that, for a given value of P/P_{eq} , β is a decreasing function of temperature.
233 As will be analyzed in detail below (section V), this peculiar dependence on temperature
234 can be explained by means of a reaction mechanism consisting not just of chemical decom-
235 position but also CO_2 desorption and an exothermic transformation of CaO structure to
236 its final stable form. Arguably, the exothermicity of CaO structural transformation might
237 contribute to the auto-catalytic effect inferred from the dependence of the conversion rate
238 on α .

239 Let us now focus on the analysis of the time evolution of CaO crystal structure during
240 decarbonation. The diffractograms obtained during decarbonation are useful to address the
241 question on a possible preferential growth of the CaO crystal structure along poorly reac-
242 tive (200) planes, which has been suggested in recent theoretical works as a cause of its
243 very low reactivity when calcination is carried out at high CO_2 vol.% and high tempera-
244 ture [7, 32]. The ratio of CaO Bragg peak (111) intensity to CaO (200) peak intensity is
245 plotted in Fig. 6 as a function of calcination time. The horizontal dashed line indicates
246 the relative intensity given by CaO (lime) reference patterns ($I_{111}/I_{200} = 0.389$) available
247 from the Crystallography Open Database (COD) [37]. As can be seen, the relative intensity
248 measured falls to this level once decarbonation is completed, which indicates that there is
249 not a preferred orientation of crystallographic planes at the CaO surface. However, the
250 results for the tests carried out at $890^\circ\text{C}/70\%\text{CO}_2$ and $860^\circ\text{C}/50\%\text{CO}_2$ (with a noticeable
251 induction period and very slow decarbonation) illustrate that the ratio I_{111}/I_{200} is well over
252 0.389 when the CaO peaks start to appear. The diffractograms obtained from these tests
253 are plotted in Fig. 3. Interestingly, the peaks located at the positions indicative of the CaO
254 cubic lattice become already visible before CaCO_3 peaks intensity start to decline. This may
255 be seen more clearly in Fig. 4, where the intensities of the Bragg CaCO_3 and CaO reflection

256 peaks are plotted as a function of time for the calcination test at $860^{\circ}\text{C}/50\%\text{CO}_2$. CaO
257 reflection peaks appear 12 min after the calcination temperature is reached, but the decline
258 of CaCO_3 (211) main peak intensity is not seen until 10-15 min later. For calcination at
259 $890^{\circ}\text{C}/70\%\text{CO}_2$ the intensity of the CaCO_3 peaks remains practically constant during the
260 whole test whereas CaO peaks are clearly identifiable from $t \simeq 40$ min. These anomalies
261 may be related to the formation of an intermediate CaO^* metastable structure (as early hy-
262 pothesized by Hyatt et al. [9]) yielding reflections at the same angles that the parent CaCO_3
263 rhombohedral structure. Some works based on ex-situ XRD conventional analysis of cal-
264 cined single CaCO_3 crystals under vacuum suggested that the metastable CaO^* form has the
265 same structure of the cubic CaO stable lattice [18, 24, 38, 39]. However, the crystallographic
266 relationships of the transformation are difficult to be drawn from either in-situ or ex-situ
267 conventional XRD analysis [1]. Recent observations from transmission electron microscopy
268 coupled with selected area electron diffraction (TEM-SAED) and 2D-XRD analyses on the
269 decomposition of calcite single crystals [1] have confirmed that the reaction involves a crys-
270 tallographic structural transformation as in the general class of topotactic transformations.
271 Accordingly, decarbonation was seen to be initiated by the development of a mesoporous
272 structure consisting of rod-shaped CaO^* nanocrystals on each rhombohedral cleavage face
273 of the calcite pseudomorph. Subsequently, metastable CaO^* nanocrystals underwent ori-
274 ented aggregation driven by surface attractive forces and became afterwards sintered. As
275 the mesopores between the rod-shaped CaO^* nanocrystals were closed, CO_2 was desorbed to
276 complete the transformation by the nucleation of stable CaO cubic crystals [1]. The kinetics
277 of the transformation was observed to be determined by chemical decomposition since the
278 desorption and structural transformation process proceeded extremely fast in the calcination
279 tests, which were carried out under vacuum. Unfortunately, application of TEM-SAED to

280 elucidate the details of the topotactic transformation is not feasible under high CO₂ partial
 281 pressure (technical progress in this direction would be a challenging task to pursue in future
 282 works).

283 IV. TG ANALYSIS

284 Figure 7 shows the thermograms obtained from the TGA calcination tests. As seen
 285 in the inset, the time evolution of CaCO₃ conversion α derived from these tests ($\alpha =$
 286 $(100/44)|\Delta wt|/wt_0$ where wt_0 is the initial CaCO₃ weight and Δwt is the weight loss) can
 287 be well fitted by a sigmoidal equation

$$\alpha = \frac{1}{1 + \exp(-\beta(t - t_0))} \Leftrightarrow \frac{d\alpha}{dt} = f(\alpha)\beta(T, P) \quad (5)$$

288 with $f(\alpha) = \alpha(1 - \alpha)$ according to a Prout-Tompkins mechanistic rate-equation and in
 289 agreement with Eq. 4 derived from the in-situ XRD analysis. A good fit is also obtained us-
 290 ing the Avrami-Erofeev expression ($f(\alpha) = n(1 - \alpha) [-\ln(1 - \alpha)]^{1-1/n}$), which is extensively
 291 employed in kinetic studies [40, 41] and, as the Prout-Tompkins expression, also captures
 292 the existence of an induction period after which the reaction is started in structural defects.
 293 However, our main goal in the present work is not to analyze in detail the mechanistic-rate
 294 function $f(\alpha)$ that better fits to the data but the dependence of the decarbonation rate con-
 295 stant (β in Eq. 5) on temperature and CO₂ partial pressure. For this purpose, conversion
 296 time evolution data have been fitted to the simpler sigmoidal equation.

297 Figure 7 shows, also in qualitative agreement with the results derived from the in-situ
 298 XRD analysis, that decarbonation at close to equilibrium conditions (high CO₂ pressures
 299 and high temperatures) is slowed down as the temperature is increased. For a given value

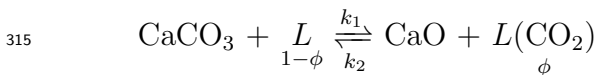
300 of conversion, the decarbonation rate $r \propto \beta$ is a decreasing function of temperature if P/P_{eq}
 301 is kept at a constant value.

302 V. REACTION KINETICS

303 According to the TGA and in-situ XRD analysis results presented, the conversion rate
 304 ($d\alpha/dt$) can be expressed as the product of the functions $f(\alpha) \simeq \alpha(1 - \alpha)$ and $\beta(T, P)$,
 305 the former one conforming to a Prout-Tompkins mechanistic model at the conditions of our
 306 experiments. We now focus on the formulation of a theoretical model for the dependence
 307 of the reaction rate on temperature T and CO_2 partial pressure, which can be retrieved
 308 experimentally from the separate function $\beta(T, P)$.

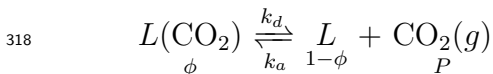
309 Let us assume the ideal situation of an infinite plane surface of a CaCO_3 solid undergoing
 310 decarbonation at uniform gas pressure and temperature. The kinetics of unimolecular surface
 311 reactions at these ideal conditions is often described by a mechanistic model consisting of
 312 chemical decomposition and desorption. Following this general concept, surface chemical
 313 decomposition gives rise to CaO and adsorbed CO_2 , which is then desorbed from the surface:

314 1. Chemical decomposition



$$316 \quad \text{Rate: } r_1 = k_1(1 - \phi) - k_2\phi$$

317 2. Desorption



$$319 \quad \text{Rate: } r_d = k_d\phi - k_a(1 - \phi)P$$

320 Here L represents an active site and $L(\text{CO}_2)$ denotes an active site filled with a molecule
 321 of CO_2 that remains adsorbed after decomposition, ϕ is the fraction of active sites covering

322 the surface which are occupied by CO₂, $(1 - \phi)$ is the fraction of active sites empty, and
 323 k_i are the reaction rate constants. The activities of the solids are equal to 1. Thus, the
 324 reaction rate would be determined by the fraction of active sites filled ϕ (either by chemical
 325 decomposition or adsorption), the gaseous CO₂ partial pressure P and the reaction rate
 326 constants.

327 According to the microscopic reversibility general principle, the state of equilibrium is
 328 reached when the average rate of any process in each elementary step is equal to the aver-
 329 age rate of its reverse process, which translated to decarbonation/carbonation and desorp-
 330 tion/adsorption means that $r_1 = r_d = 0$ at equilibrium ($\phi = \phi_{eq}, P = P_{eq}$):

$$k_1(1 - \phi_{eq}) = k_2\phi_{eq} \quad (6)$$

$$k_a(1 - \phi_{eq})P_{eq} = k_d\phi_{eq} \quad (7)$$

331 Thus,

$$P_{eq}(\text{atm}) = \frac{k_1k_d}{k_2k_a} = K_1K_d \quad (8)$$

332 where $K_1 = k_1/k_2$ and $K_d = k_d/k_a$ are the decomposition and desorption thermodynamic
 333 equilibrium constants, respectively, that can be expressed by means of the van't Hoff equa-
 334 tion:

$$K_1 = A_1 \exp(-\Delta_1H^0/RT) \quad (9)$$

$$K_d = A_d \exp(-\Delta_dH^0/RT) \quad (10)$$

335 where Δ_1H^0 and Δ_dH^0 are the standard enthalpy change for decomposition and des-
 336 orption, respectively. The pre-exponential factors are given by $A_1 = \exp(\Delta_1S^0/R)$ and

337 $A_d = \exp(\Delta_d S^0/R)$, where $\Delta_1 S^0$ and $\Delta_d S^0$ are the standard entropy changes of decomposi-
 338 tion and desorption, respectively.

339 Using the empirical equation for P_{eq} (Eq. 3) in Eq. 8, the standard enthalpy and entropy
 340 changes for the overall decarbonation reaction would be $\Delta_r H^0 = \Delta_1 H^0 + \Delta_d H^0 = 170.2$
 341 kJ/mol and $\Delta_r S^0 = \Delta_1 S^0 + \Delta_d S^0 = 145.7$ J/mol-K, which are close to the values of
 342 the standard enthalpy and entropy of the overall reaction derived from thermodynamic
 343 analysis ($\Delta_r H^0 \simeq 177.8$ kJ/mol and $\Delta_r S^0 \simeq 160.4$ J/mol-K) [2, 11, 42]. Desorption is
 344 normally an endothermic process ($\Delta_d H > 0$ with little variation on temperature) as it
 345 involves overcoming a physical bond between the solid surface and the gas usually arising
 346 from attractive van der Waals forces. Since these forces are much less strong than chemical
 347 bonding, desorption enthalpy changes are low (of the order of 20 kJ/mol) as compared with
 348 the enthalpy change associated to chemical decomposition [43]. Taking the enthalpy change
 349 of CO₂ desorption as $\Delta_d H^0 = 20$ kJ/mol, the value of the decomposition enthalpy change
 350 would be $\Delta_1 H^0 \simeq 150$ kJ/mol.

351 The pseudo-steady state hypothesis states that there is not a net accumulation of reactive
 352 intermediates [44], which implies in our case that the increase rate of the fraction of active
 353 sites filled with CO₂ by decomposition must equal the rate of desorption ($r_1 = r_d$):

$$\frac{d\phi}{dt} = 0 \Rightarrow \phi = \frac{k_1 + k_a P}{k_1 + k_2 + k_d + k_a P} \quad (11)$$

354 Let us analyze the dependence of the reaction rate on temperature and CO₂ partial
 355 pressure. In most gas-solid heterogenous reactions that are not diffusion-limited, desorption
 356 is usually a fast process as compared to chemical decomposition ($k_1, k_2 \ll k_d, k_a P$). Thus,
 357 from Eq. 11 it is

$$\phi \approx \frac{k_a P}{k_d + k_a P} = \frac{K_a P}{1 + K_a P} \quad (12)$$

358 where $K_a = 1/K_d$. Note that Eq. 12 conforms to the Langmuir isotherm equation for
 359 adsorption. Using Eq. 8 the overall reaction rate can be written as

$$r \approx r_1 = k_1(1 - \phi) - k_2\phi = k_1 \left(1 - \frac{P}{P_{eq}}\right) (1 - \phi) \approx k_1 \left(1 - \frac{P}{P_{eq}}\right) \frac{1}{1 + K_1 P/P_{eq}} \quad (13)$$

360 The rate constant k_1 follows an Arrhenius law

$$k_1 = a_1 \exp(-E_1/RT) \quad (14)$$

361 where $E_1 > 0$ is the activation energy for decomposition and a_1 is a pre-exponential factor,
 362 which yields

$$r \approx a_1 \exp(-E_1/RT) \left(1 - \frac{P}{P_{eq}}\right) \frac{1}{1 + A_1 \exp(-\Delta_1 H^0/RT) P/P_{eq}} \quad (15)$$

363 At very low CO_2 partial pressures or low calcination temperatures it is $K_a P = K_1 P/P_{eq} \ll$
 364 1 and the fraction of active sites filled with adsorbed CO_2 molecules is small ($\phi \ll 1$ in Eq.
 365 12). In this limit the reaction rate predicted is

$$r \approx a_1 \exp(-E_1/RT) \left(1 - \frac{P}{P_{eq}}\right) \quad (16)$$

366 which conforms to Eq. 2 commonly employed as a good fit to experimental data on the rate
 367 of decarbonation (usually performed at $P \ll P_{eq}$) and yielding activation energies around
 368 the overall reaction enthalpy change (although in a widely scattered range between 100 and
 369 230 kJ/mol [22]). Thus, the reaction rate increases with temperature following an Arrhenius
 370 law controlled by the activation energy of chemical decomposition E_1 .

371 In the opposed limit ($K_a P = K_1 P / P_{eq} \gg 1 \leftrightarrow (1 - \phi) \approx 1 / (K_a P)$), which may be
 372 met only at very high temperatures ($K_1 \gg 1$) and not small CO₂ partial pressures, the
 373 predicted reaction rate would be

$$r \approx a_2 \exp(-E_2 / RT) \left(\frac{P_{eq}}{P} - 1 \right) \quad (17)$$

374 where $E_2 = E_1 - \Delta_1 H^0$ is the activation energy for the carbonation chemical reaction.

375 Since the activation energy usually measured for calcination at $P / P_{eq} \ll 1$ is close to
 376 the overall reaction enthalpy change derived from thermodynamic analysis ($E_1 \simeq \Delta_r H^0$),
 377 it might be thought that the activation energy for carbonation E_2 is close to zero as pos-
 378 tulated in previous works [45] where the desorption/adsorption step is obviated. However,
 379 recent experimental measurements [42] on the carbonation kinetics yield a non-negligible
 380 carbonation activation energy $E_2 = 24 \pm 6$ kJ/mol. This value is entirely consistent with
 381 a decomposition enthalpy change $\Delta_1 H^0 = \Delta_r H^0 - \Delta_d H^0 \simeq 150$ kJ/mol where $\Delta_d H^0 \simeq 20$
 382 kJ/mol as assumed above. Thus, Eq. 17 would predict also an increase of the reaction rate
 383 with temperature at high CO₂ pressures but at a lower rate ($E_2 \simeq 20$ kJ/mol) as compared
 384 with the predicted rate from Eq. 16.

385 Let us now explore the possibility that the slowest rate-limiting step in decarbonation is
 386 CO₂ desorption ($k_1, k_2 \gg k_d, k_a P$). In that case the overall reaction rate would be given
 387 by the rate of desorption

$$r \approx k_d \phi - k_a (1 - \phi) P \quad (18)$$

388 with the fraction of active sites filled with CO₂ determined by the chemical reaction rate
 389 constants (Eq. 11):

$$\phi \approx \frac{k_1}{k_1 + k_2} = \frac{1}{1 + 1/K_1} \quad (19)$$

390 Thus,

$$r \approx k_d \left(1 - \frac{P}{P_{eq}}\right) \phi \approx a_d \exp(-E_d/RT) \left(1 - \frac{P}{P_{eq}}\right) \frac{1}{1 + \exp(\Delta_1 H^0/RT)/A_1} \quad (20)$$

391 where E_d is the activation energy for desorption and a_d is a pre-exponential factor. According
 392 to Eq. 19, in the limit $K_1 = K_a P_{eq} \gg 1$ the fraction of active sites occupied by CO₂ would
 393 be large ($\phi \simeq 1$) and the reaction rate would depend mainly on T through k_d increasing with
 394 temperature following an Arrhenius law determined by the activation energy of desorption
 395 E_d :

$$r \approx a_d \exp(-E_d/RT) \left(1 - \frac{P}{P_{eq}}\right) \quad (21)$$

396 Since the activation energy of adsorption E_a is in general not appreciable [43], it would be
 397 $E_d = E_a + \Delta_d H^0 \simeq 20$ kJ/mol.

398 In the limit $K_1 = K_a P_{eq} \ll 1$ it is $\phi \ll 1$ (Eq. 19), and the reaction rate would be

$$r \approx a_d A_1 \exp(-(E_d + \Delta_1 H^0)/RT) \left(1 - \frac{P}{P_{eq}}\right) \quad (22)$$

399 where $E_d + \Delta_1 H^0 \simeq \Delta_r H^0 \simeq 170$ kJ/mol.

400 **A. The role of structural transformation**

401 None of the above mechanisms would predict a decrease of the reaction rate with temper-
 402 ature at constant P/P_{eq} as inferred from our calcination tests nearby equilibrium. However,

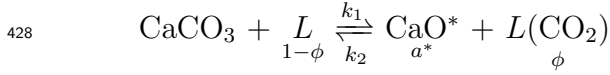
403 the experimentally observed transformation from the metastable CaO form (CaO*) to the
 404 stable CaO form as CO₂ is desorbed has not been yet considered. As detailed in the study re-
 405 ported in [18] on calcite decarbonation under vacuum, desorbed CO₂ molecules must escape
 406 out from the reaction surface by diffusion through the metastable CaO* porous network. An
 407 estimation of the fraction of desorbed CO₂ molecules that passes across a porous barrier is
 408 given by [18]

$$\Lambda = \frac{\Gamma}{\Gamma + \epsilon} \quad (23)$$

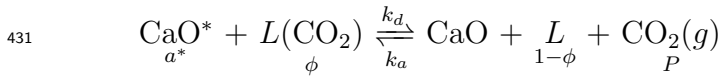
409 where Γ is the probability that a CO₂ molecule emerges out of the barrier by diffusion
 410 without coming back and ϵ is the probability that a returned CO₂ molecule reacts back.
 411 According to the principle of microscopic reversibility, the partial pressure of CO₂ inside the
 412 CaO* pores (P_{int}) would be close to the equilibrium pressure $P_{int} \sim P_{eq}$ regardless of the
 413 CO₂ partial pressure in the surrounding environment P . If P is very small ($P/P_{eq} \ll 1$), it
 414 would be $P_{int} \gg P$ and the value of Γ may be simply estimated from a Knudsen diffusion
 415 process as the ratio of the pore size to the barrier thickness, which is typically much larger
 416 than ϵ [18]. Therefore, desorption can be dismissed for calcination under vacuum as recently
 417 confirmed by in-situ observations showing that there is no significant resistance against
 418 the outwards diffusion of CO₂, which was seen to escape out from the porous metastable
 419 CaO* very quickly [1]. Thus, chemical decomposition determines the reaction kinetics for
 420 calcination under very small CO₂ partial pressures ($P/P_{eq} \ll 1$). The scenario may change
 421 however for calcination at high CO₂ partial pressures. Under this condition, the leakage of
 422 CO₂ molecules through the metastable structure would be hampered according to Fick's law
 423 since the gradient between the CO₂ pressure inside the porous network and outside is small.
 424 CO₂ desorption and the concomitant transformation of the metastable CaO* to CaO should

425 be considered as a further necessary step of the reaction for decarbonation to be completely
 426 achieved:

427 **1. Chemical decomposition**



430 **2. Desorption and structural transformation**



433 where a^* stands for the activity of the metastable CaO^* form. In general, whenever the
 434 direct solid product of a decomposition reaction is a metastable crystal modification or an
 435 amorphous form, the activity of this solid cannot be taken as unity but [46]

$$a^* = \exp(\Delta G_*/RT) \quad (24)$$

436 where $\Delta G_* = \Delta H_* - T\Delta S_*$ is the positive free energy of formation of the metastable form
 437 from the stable form. The enthalpy change ΔH_* would be the energy relieved when the
 438 metastable CaO^* structure collapses after desorption into the stable CaO structure, which
 439 has been estimated elsewhere as $\Delta H_* \sim 50$ kJ/mol from calcination tests under vacuum
 440 [18, 46, 47]. Formally, the predicted rates are the same as above but replacing the rate
 441 constants k_2 and k_d by $k_2 a^*$ and $k_d a^*$, respectively. The overall reaction rate at high values
 442 of P/P_{eq} would be then

$$r \approx a_d A_* \exp(-(E_d - \Delta H_*)/RT) \left(1 - \frac{P}{P_{eq}}\right) \phi \quad (25)$$

$$\phi \approx \frac{1}{1 + \exp((\Delta_1 G^0 + \Delta G_*)/RT)} \quad (26)$$

443 where $A_* = \exp(-\Delta S_*/R)$ and $\Delta_1 G^0 = \Delta_1 H^0 - T\Delta_1 S^0$. In the limit $\phi \simeq 1$, which would
 444 be the case at high temperatures, the reaction rate would be given by

$$r \approx a_d A_* \exp(-(E_d - \Delta H_*)/RT) \left(1 - \frac{P}{P_{eq}}\right) \quad (27)$$

445 Since expectedly it is $E_d - \Delta H_* < 0$, the reaction rate would be decreased with temperature
 446 at constant P/P_{eq} as observed in our tests. As the temperature is lowered down the fraction
 447 ϕ decreases and in the limit $\phi \ll 1$ ($\exp((\Delta_1 G^0 + \Delta G_*)/RT) \gg 1$) the reaction rate
 448 predicted would be

$$r \approx a_d A_1 \exp(-(E_d + \Delta_1 H^0)/RT) \left(1 - \frac{P}{P_{eq}}\right) \quad (28)$$

449 which decreases with temperature ($E_d + \Delta_1 H^0 \simeq 170$ kJ/mol). According to this mechanism
 450 we would observe an increase of the reaction rate with $1/T$ at high temperatures with a
 451 progressively decreasing rate as $1/T$ is increased and ϕ decreases. At a certain critical
 452 temperature the reaction rate reaches a maximum and turns to decrease with $1/T$.

453 Let us compare the α -independent reaction rate factor $\beta(T, P) \sim r$ measured from
 454 our XRD and TGA tests with the reaction rates theoretically predicted. Measured val-
 455 ues of $\beta/(1 - P/P_{eq})$ are plotted in Fig. 8 as a function of $1/T$. The trends plotted
 456 ($r \propto \exp(-E/RT)$) are the theoretical predictions from Eq. 27 (using $E = -30$ kJ/mol
 457 and -200 kJ/mol), Eqs. 17 and 21 ($E = 20$ kJ/mol), and Eqs. 16, 22 and 28 ($E = 170$
 458 kJ/mol). In spite of the data scatter, Fig. 8 shows that for high temperatures ($T \gtrsim 830^\circ\text{C}$)

459 the reaction rate clearly increases with $1/T$ in agreement with Eq. 27 ($\phi \simeq 1$). A good fit
460 is obtained for $E = -200$ kJ/mol suggesting a value for the enthalpy change of structural
461 transformation $\Delta H_* \sim 220$ kJ/mol. Interestingly, it is seen in Fig. 8 that the increase of
462 the reaction rate with $1/T$ slows down at lower temperatures which could be explained by a
463 decrease of ϕ with $1/T$ (Eq. 26). In our tests, the ratio P/P_{eq} varies in a window between 0.6
464 and 0.85. Further experiments in narrower windows of P/P_{eq} might help reducing the exper-
465 imental data scatter as well as identifying more clearly the role of the diverse mechanisms on
466 the reaction rate. The difficulty of these measurements resides in the control of phenomena
467 such as temperature gradients in the solid or internal mass/heat transfer effects that are
468 specially relevant for calcination under high CO_2 partial pressures [16, 48]. For example,
469 thermal diffusion may affect the reaction kinetics due to temperature differences of a few
470 $^\circ\text{C}$ between the interior of the solid and its external surface caused by the endothermicity of
471 the reaction [48]. This can be relevant if the reaction is hindered by outwards CO_2 diffusion
472 when the CO_2 partial pressure in the surrounding environment is close to the equilibrium
473 pressure. To overcome this burden and simplify the kinetic analysis most studies reported
474 in the literature are carried out in the limit $P/P_{eq} \ll 1$. Yet the study of calcination at
475 high CO_2 pressure and high temperatures has gained a remarkable interest from recently
476 emerged applications such as the Ca-looping for post-combustion CO_2 capture. Our results
477 show that, at these conditions, the decarbonation rate is decreased with temperature (at
478 least in a certain range of high temperatures/high CO_2 partial pressures). Additional re-
479 search on the kinetics of calcination nearby equilibrium should be pursued in future studies
480 to further explore this result.

481 VI. CaO CHARACTERIZATION

482 In this section we investigate the structural properties and chemical reactivity of CaO
483 resulting from limestone calcination as influenced by the calcination temperature and CO₂
484 partial pressure at the conditions of our tests close to equilibrium.

485 A. CaO crystallite size

486 In-situ XRD tests allow us obtaining the time evolution of the CaO coherently diffracting
487 domain size (usually known as crystallite size L_c) by means of the Scherrer equation

$$L_c = \frac{\kappa \lambda}{\beta \cos \theta} \quad (29)$$

488 where $2\theta \simeq 37.1^\circ$ is the Bragg angle of the most intense CaO reflection peak (200), κ is a
489 dimensionless shape factor ($\kappa = 0.89$ for the CaO cubic structure), and β (in radians) is the
490 line broadening at half the maximum intensity (full width at half maximum FWHM). Line
491 broadening has been corrected by the instrumental width $\beta_0 \simeq 0.132$, which was obtained
492 from the XRD pattern of certified LaB₆. Thus, it is $\beta = [\beta_M^d - \beta_0^d]^{1/2}$, where β_M is the
493 experimentally measured FWHM and $d = 2$ since the peak shape conforms approximately
494 to a Gaussian distribution.

495 Figure 9 shows the time evolution of the CaO crystallite size L_c during calcination. We
496 see that L_c is mainly determined by its initial value and changes only slightly as calcination
497 progresses. The most determining parameter is the CO₂ partial pressure, whose increase
498 leads in general to an increase of L_c . For values of the CO₂ vol.% below 30%, L_c shows a
499 moderate increase with the calcination time and increases as the calcination temperature is
500 risen. On the other hand, a diverse trend is observed for the samples calcined at higher CO₂

501 vol.%. In this range of high CO₂ partial pressures, L_c reaches a relatively high value as soon
502 as CaO peaks are detected and decreases slightly with the calcination time. Moreover, for a
503 given value of high CO₂ vol.%, L_c is increased as the calcination temperature is diminished.
504 For example, the average value of L_c is 34 nm for the sample calcined at 900°C under
505 70%CO₂ whereas it is $\langle L_c \rangle \simeq 41$ nm when the calcination temperature is 890°C and the
506 reaction kinetics is considerably slowed down (see Figs. 5 and 7). This observation supports
507 a sintering mechanism near equilibrium according to which the nascent CaO crystallites are
508 initially formed by aggregation of metastable CaO* nanocrystals and sintering afterwards.
509 Under high CO₂ vol.%, the aggregation step would be enhanced by a slower reaction kinetics
510 at smaller temperatures since CO₂ desorption and structural transformation are hindered.
511 Moreover, a high fraction of active sites filled with CO₂ molecules adsorbed on the surface of
512 the CaO* nanocrystals during this very slow process ($\phi \simeq 1$) would give rise to a significant
513 increase of their surface energy [49] and therefore would enhance the attractive force between
514 them. This would yield an enlargement of the CaO coherent crystal length when the unstable
515 structure collapses into the stable CaO form and CO₂ molecules are desorbed. On the other
516 hand, the dominant mechanism at low CO₂ partial pressures for CaO crystal growth would
517 be sintering of the nanocrystals by lattice diffusion which is promoted by an increase of
518 temperature. Accordingly, we see larger crystallites as the temperature is increased in the
519 calcination tests at low CO₂ vol.%.

520 **B. CaO sintering**

521 Representative SEM images of samples calcined in the XRD chamber at diverse condi-
522 tions of temperature and CO₂ vol.% are displayed in Fig. 10. As may be seen, an increase
523 of temperature and CO₂ vol.% yields a noticeable decrease of porosity and an increase of

524 grain size as well documented from previous studies (albeit in previous works calcination
 525 conditions are generally far from equilibrium: $P/P_{eq} \ll 1$) [21, 50, 51]. Average values of
 526 the grain size d derived from a statistical analysis of SEM images are plotted in Fig. 11a
 527 showing a clear correlation between d and the CO₂ partial pressure which fits approximately
 528 to a linear increase law. In contrast with the decrease observed for the crystallite size L_c
 529 with temperature at high CO₂ partial pressure, we see that d is an increasing function of
 530 temperature independently of the CO₂ vol.% (see the inset of Fig. 11a). After formation of
 531 the stable CaO crystallites, the sintering process should be driven by the subsequent agglom-
 532 eration of these crystallites into polycrystalline CaO grains and the parallel closure of small
 533 pores. Further agglomeration of the polycrystalline CaO grains as calcination progresses
 534 would be favored by temperature enhanced lattice diffusion. Figure 11b demonstrates a
 535 clear quantitative correlation between the ratio of CaO grain size to crystallite size with the
 536 CO₂ vol.% (CO₂ vol.% $\approx P$ (kPa) in our tests at atmospheric pressure), which is rather well
 537 adjusted by the linear law

$$\frac{d}{L_c} \simeq 1 + 0.4P \quad (30)$$

538 Extrapolating this law to $P = 0$ it is predicted $d_0 \simeq L_{c0}$, which suggests that, in the absence
 539 of CO₂, sintering is precluded and the CaO structure resulting from calcination would consist
 540 of mono-crystalline CaO nanograins with very high surface area as observed in experiments
 541 where calcination is carried out under vacuum (at temperatures as high as 1050°C) [47]. As
 542 was shown in [47], XRD patterns of CaO resulting from calcination under vacuum exhibit
 543 very weak diffraction peaks indicative of the production of CaO crystallites of size ~ 10
 544 nm regardless of the calcination temperature. This supports the argument that aggregation
 545 of the CaO* nanocrystals, which is enhanced by promoted surface energy due to adsorbed

546 CO₂, plays a main role on the enhanced sintering of CaO calcined under high CO₂ partial
547 pressure.

548 The agglomeration and growth of CaO polycrystalline grains must be accompanied by the
549 closure of small pores and therefore by a reduction of the surface area. Pore size distributions
550 obtained for our calcined samples from N₂ physisorption (77 K) analysis are shown in Fig.
551 12. As can be seen, the pore area is drastically reduced as the CO₂ vol.% is increased above
552 30%, which causes that a major fraction of the pores grow up to a size larger than the
553 upper limit detectable by the N₂ physisorption technique (~200 nm). Consequently, values
554 of the BET surface area obtained S_{BET} for the samples calcined under CO₂ vol.% above
555 50% are below the accuracy of the technique, which is about 1 m²/g. Alternatively, a rough
556 estimation of the surface area may be inferred by approximating the CaO grains of size d
557 derived from the SEM analysis (Fig. 11) to smooth spheres [50], which gives $S_d \sim 6/(\rho_{CaO}d)$
558 where $\rho_{CaO} = 3.37$ g/cm³ is CaO solid density. Figure 13a shows S_{BET} and S_d as a function
559 of grain size. Taking into account the experimental indeterminacy, there is an acceptable
560 agreement between both data sets. The surface area of the samples calcined under CO₂
561 vol.%>50% is estimated to be close to the residual surface area for limestone derived CaO
562 ($S_r \sim 1$ m²/g) [52]. Additional physisorption tests on the calcined samples were carried out
563 in our work using Kr (77 K) instead of N₂, which generally gives better results for samples
564 with low surface area. Values measured of S_{BET} using Kr are plotted in Fig. 14 showing
565 that CaO attains a residual surface area as expected of about 1 m²/g at severe calcination
566 conditions.

567 Most of the data published in the literature on the variation of CaO surface area ΔS
568 with calcination time t_s [21] conforms reasonably well to the German-Munir equation [53],

$$\frac{\Delta S}{S_0} = (K_s t_s)^{1/\gamma_s} \quad (31)$$

569 where S_0 is the initial surface area, the sintering constant K_s follows an Arrhenius law
 570 type dependence on temperature and the exponent γ_s is related to the main mechanism
 571 responsible for sintering. The German-Munir model assumes that CaO grains with initially
 572 spherical shape sinter by formation of a neck at contact points, which grows in diameter
 573 as matter is transported to the neck region by several possible mechanisms. For calcina-
 574 tion in an inert atmosphere, the transport mechanism depends generally on the calcination
 575 temperature as compared to the melting temperature T_m of the material [54]. In the usual
 576 range of calcination temperatures for CaO ($T_m = 2886$ K) between 700°C and 1000°C , it
 577 is $0.33T_m \lesssim T \lesssim 0.44T_m$ (in K), which would imply that sintering should occur by surface
 578 diffusion of chemical constituents [54]. Sintering by lattice diffusion is initiated in most
 579 materials at the so-called Tamman temperature T_t (around half the melting temperature in
 580 K), which is $T_t \simeq 1170^\circ\text{C}$ for CaO [54]. Diffusion of chemical species across the crystalline
 581 lattice would become noticeable only above this temperature, which is well over the range of
 582 common limestone calcination temperatures. Yet, sintering rates of limestone derived CaO
 583 for calcination under pure N_2 (in the temperature range between 700°C and 1100°C) agrees
 584 with the prediction by Eq. 31 for $\gamma_s \simeq 2.7$ suggesting that transport of matter does occur
 585 by lattice diffusion mechanism [50], which is attributed to the acceleration of solid-state-
 586 diffusion by impurities and lattice defects. Results from calcination of ultrapure CaCO_3
 587 large monocrystals yielded slower sintering rates more consistent with surface (instead or
 588 lattice) diffusion [50] as expected. On the other hand, CaO sintering is greatly enhanced by
 589 the presence of CO_2 in the calcination atmosphere, which is a well documented observation
 590 [21, 51, 55, 56] albeit most experiments are carried out in the regime $P/P_{eq} \ll 1$. The

591 sintering constant K_s and exponent γ_s that fit most of the experimental data are given by

$$K_s = 1.08 \times 10^8 P^{0.558} \exp(-30000/T) \quad (32)$$

$$\gamma_s = 44.1(0.8 \ln P - 1) \exp(-4140/T) \quad (33)$$

592 (missprints in the equations presented in the original work [51] are noted in a later review
 593 [21]). Here P is in Pa, the temperature T is in K and K_s in min^{-1} . Experimental data are
 594 fitted by using values of γ_s well over 10, which indicates a strong influence of extraordinary
 595 sintering mechanism(s) induced by the presence of CO_2 not well understood yet. Likewise,
 596 water vapor leads to a marked catalyzing effect of sintering [51].

597 The German-Munir model [53] is based on the assumption that the nascent CaO forms an
 598 open array of grains that coalesce via neck formation and growth at contact points. Under
 599 the restriction $|\Delta S/S_0| < 0.5$, the curvature gradient in the neck region yields a relative
 600 decrease of the surface area given by Eq. 31. Equations 31-33 yield unreasonable values for
 601 $|\Delta S/S_0|$ in the CO_2 partial pressure and temperature conditions of our tests. Moreover, Eq.
 602 31 cannot account for the approach to a residual value S_r for long sintering times as observed
 603 experimentally. This is taken into account by the empirical general power law expression
 604 (GPLe) originally derived to describe the sintering and deactivation of supported metal
 605 catalysts [57]

$$-\frac{d}{dt} \frac{S}{S_0} = k_s \left(\frac{S}{S_0} - \frac{S_r}{S_0} \right)^m \Rightarrow S \approx S_0 \frac{1 + k_s t_s S_r / S_0}{1 + k_s t_s} \quad (34)$$

606 where it has been applied $m = 2$ valid for sintering processes governed by lattice diffusion
 607 [57], k_s is a sintering constant and we have used $S_r/S_0 \ll 1$. Equation 34 has been
 608 employed to fit experimental data on CaO sintering [21, 58] with k_s following an Arrhenius

609 type law at low CO₂ partial pressures [21]. Equation 34 has served to predict the loss of
 610 CaO carbonation activity in the surface reaction controlled regime as it is subjected to a
 611 long series of carbonation/calcination cycles by assuming that the carbonation reactivity
 612 scales proportionally to the surface area [59, 60] (this point will be addressed below in
 613 further detail). The surface area of the nanostructured CaO just before sintering starts
 614 ($S = S_0$) has been estimated elsewhere as $S_0 = 104 \text{ m}^2/\text{g}$ from measurements on samples
 615 taken immediately after calcination in air at 700°C [50], which agrees with estimations
 616 on the surface area of the metastable CaO* nanocrystals [18, 61] (in agreement with the
 617 prediction $d_0 \simeq L_{c0}$ from Eq. 31). Using $S_0 = 104 \text{ m}^2/\text{g}$ and $S_r = 1 \text{ m}^2/\text{g}$ in Eq. 34 we
 618 find a good fit to our experimental data on S (Fig. 13b) for a sintering constant k_s ten
 619 times the sintering constant K_s reported for relatively low CO₂ partial pressures (Eq. 32).
 620 A possible explanation for the catalyzing effect of CO₂ on sintering (particularly relevant
 621 at CO₂ pressures near the equilibrium pressure) is that CO₂ molecules physically adsorbed
 622 on the surface of the grains leads to a great enhancement of surface energy, which would
 623 promote the agglomeration of the grains.

624 Further simplification of Eq. 34 allowed by $S_r/S_0 \sim 0.01 \ll 1$ leads to the simple
 625 equation $S/S_0 \approx 1/(1 + k_s t_s)$ for short sintering times. Since $S \propto d$, we arrive also at
 626 $d/d_0 \simeq (1 + k_s t_s)$ with $k_s \simeq 10^9 \times P^{0.5} \exp(-E_s/RT) \text{ min}^{-1}$, an activation energy for
 627 sintering $E_s \simeq 250 \text{ kJ/mol}$, and $d_0 \simeq 15 \text{ nm}$ for the CaO grain size in the absence of
 628 CO₂ in the calcination atmosphere (estimated using $S_0 \sim 100 \text{ m}^2/\text{g}$ for uniform spheres
 629 with no connecting necks) and equal to CaO crystallite size. From a practical perspective,
 630 sintering at high CO₂ partial pressure might be mitigated by placing in the lattice thermally
 631 stable inert nanocrystals that would minimize aggregation of the CaO* nanocrystals and
 632 CaO grains. This could be for example the role played by MgO nanocrystallites in calcined

633 dolomite ($\text{CaMg}(\text{CaCO}_3)_2$) [30] and mayenite nanocrystallites in synthetic CaO/mayenite
634 composites [62], which help mitigating CaO sintering as observed experimentally.

635 C. CaO reactivity

636 Let us finally analyze the effect of calcination conditions on the reverse carbonation
637 reaction, which would take place if the temperature and CO_2 pressure are changed to shift
638 the reaction towards carbonation. Carbonation of CaO is initiated by a reaction-controlled
639 phase on the surface of the CaO grains until a thin layer of CaCO_3 (between 30 and 50
640 nm thick [35, 63, 64]) is developed, which leads to a much slower phase driven by the
641 counter-current diffusion of inward CO_3^{2-} anion groups and outward O^{2-} anions through the
642 carbonated layer [35, 63, 65]. From our in-situ XRD analysis we may infer that the CaO
643 structure that results after full calcination does not have a preferential crystallographic
644 direction oriented normal to the exposed surface, which might have an influence on the CaO
645 carbonation reactivity in the reaction controlled phase as was suggested in previous studies
646 [7, 31–33]. We now investigate whether the poor carbonation reactivity of CaO resulting
647 from calcination under high CO_2 vol.% reported in previous works [7] can be solely explained
648 by the decrease of CaO surface area as a consequence of enhanced sintering.

649 Figure 15a shows data on CaO conversion in the reaction controlled phase X_r measured
650 in our TGA tests by carbonation in-situ at $650^\circ\text{C}/15\%\text{CO}_2$ (typical conditions of post-
651 combustion CO_2 capture [2]) as a function of grain size d (derived from the SEM analysis).
652 The inset of Fig. 15a illustrates the time evolution of sample weight during carbonation.
653 As may be seen, the end of the reaction controlled fast phase and beginning of the diffusion
654 controlled slow phase is clearly distinguishable. Figure 15a demonstrates that X_r is well
655 correlated to sintering and is approximately proportional to the inverse of CaO grain size d .

656 Thus, it may be inferred that X_r scales proportionally to the CaO surface area available for
 657 carbonation as assumed in previous modeling studies [66]. Interestingly, an extrapolation of
 658 the results to the grain size lower limit suggests that all CaO available would be converted
 659 in the reaction controlled phase if grain size were below a value of around 50 nm as would be
 660 the case of CaO derived from calcination at relatively low temperature and low CO₂ partial
 661 pressure or under vacuum.

662 By assuming that for large CaO grains the reaction surface of area S is flat and that the
 663 reaction controlled phase ends up when a thin layer of thickness h is formed on the surface,
 664 CaO conversion in this phase could be estimated using the simple equation

$$X_r = \left[\frac{M_{CaO}}{M_{CaCO_3}} \rho_{CaCO_3} h \right] S \quad (35)$$

665 where M_{CaO}/M_{CaCO_3} is the ratio of CaO/CaCO₃ molecular weights and $\rho_{CaCO_3} = 2.7$
 666 g/cm³ is the CaCO₃ solid density. CaO conversion results predicted from Eq. 35, using the
 667 estimated values of surface area from grain size (S_d) and $h = 40$ nm, are plotted in Fig. 15b
 668 versus the X_r data experimentally measured. As may be seen, there is a good agreement
 669 between predicted and measured data. Equation 35 gives however unrealistic conversions
 670 above one for $S_d \gtrsim 17$ m²/g ($d \lesssim 100$ nm). In this case, the flat surface assumption leading
 671 to Eq. 35 is not justified and more sophisticated models have to be developed [35, 64,
 672 67]. Moreover, the closure of small pores by CaCO₃ limits the carbonation reaction before
 673 diffusion becomes rate-limiting.

674 Our work shows that, in the conditions of our tests, and regardless of CO₂ partial pressure
 675 and temperature, there is not a preferential growth of the CaO surface along poorly reactive
 676 (200) planes as has been suggested from theoretical studies [32]. Thus, the very small
 677 carbonation reactivity of CaO derived from calcination under high temperature and CO₂

678 concentration may be explained just by the considerable reduction of surface area as a
679 consequence of sintering. It can be noticed that CaO conversion in the reaction controlled
680 phase for the samples calcined under the most severe conditions is close to 0.1 (Fig. 15),
681 which is close to the residual conversion seen when limestone derived CaO is subjected
682 to a long series of carbonation/calcination cycles [59, 66]. Accordingly, we see that the
683 surface area of these samples calcined under harsh conditions is reduced to a value near
684 the residual value of $\sim 1 \text{ m}^2/\text{g}$ (Fig. 13). It remains to be explained the drastic drop of
685 CaO conversion experienced by samples precalcined in air and subsequently subjected to
686 carbonation/calcination cycles in which calcination is carried out under high CO_2 vol.% and
687 high temperature [7]. CaO conversion in these tests dropped in just about 10 cycles to a
688 value of about half the value of conversion corresponding to the residual CaO surface area.
689 The type of precalcination atmosphere in those tests was crucial for CaO conversion in the
690 reaction controlled phase to drop to such a small value. If precalcination was carried out also
691 under high CO_2 vol.%, CaO conversion reached a residual value close to 0.1 as corresponds to
692 CaO residual surface area. The possibility that CaO resulting from regeneration in multiple
693 carbonation/calcination tests grow preferentially along planes with low reactivity has yet
694 to be explored. At this moment, technical difficulties related to low heating rates in the
695 XRD temperature chamber precludes us from carrying out an in-situ XRD study at realistic
696 Ca-looping conditions, which necessarily imply very fast changes of temperature between
697 the carbonation and calcination stages.

698 VII. CONCLUSIONS

699 In this work we have analyzed the influence of CO_2 partial pressure on limestone de-
700 composition nearby equilibrium in order to explore the fundamental mechanisms governing

701 the reaction at these conditions. Results from in-situ XRD analysis and TGA tests show
702 that the conversion rate $d\alpha/dt$ can be expressed as the product of a conversion independent
703 reaction rate $\beta(T, P)$ and a function of conversion $f(\alpha) = \alpha(1 - \alpha)$, which conforms to a
704 Prout-Tompkins mechanistic rate-equation. The reaction rate is decreased by an increase
705 of temperature if the ratio of CO₂ partial pressure to equilibrium pressure is kept constant
706 and high ($P/P_{eq} \gtrsim 0.6$). This observation may be explained by a reaction mechanism in
707 which hindered CO₂ desorption and (exothermic) CaO*/CaO structural transformation are
708 a further necessary step for decarbonation to be completed. Arguably, the reaction would
709 be initiated after an induction period in certain active sites located at crystal defects where
710 the outwards diffusion of desorbed CO₂ is favored, which agrees with observations reported
711 elsewhere on the effect of limestone crystallinity on the reaction rate at high CO₂ partial
712 pressure [8]. Once initiated, conversion is accelerated as it progresses, presumably helped
713 by the exothermicity of the structural transformation, until it reaches a maximum rate and
714 slows down when approaching its end.

715 In regards to CaO sintering during calcination, in-situ XRD analysis and SEM obser-
716 vations show that the great reduction of CaO surface area after calcination at high CO₂
717 partial pressure and high temperature is mainly caused by CaO grain agglomeration and
718 not crystal growth. The size of CaO crystallites in the stable cubic form increase with the
719 CO₂ partial pressure from $L_c \sim 20$ nm at low pressures to $L_c \sim 40$ nm at high pressure. Van
720 der Waals attractive forces between the CaO* nanocrystals would be enhanced by adsorbed
721 CO₂ molecules whose desorption is hindered at high CO₂ partial pressure, which promotes
722 aggregation of these metastable nanocrystals and gives rise to stable CaO crystallites of
723 larger size. An extrapolation of our results gives $d_0 \simeq L_{c0}$ for calcination in the absence
724 of CO₂ ($P = 0$), which is in accordance with observations reported elsewhere on calcina-

725 tion under vacuum giving rise to a large surface area nanostructured CaO with very high
726 carbonation reactivity. According to our observations the size of stable CaO crystallites
727 do not change appreciably as the calcination time is increased, which supports the idea
728 that their formation is mainly determined by agglomeration during the transformation of
729 the metastable CaO* structure. On the other hand, the size of polycrystalline CaO grains
730 d , which would result from agglomeration and sintering of the CaO crystallites during the
731 calcination period, show a marked increase from $d \sim 50$ nm at low CO₂ partial pressure/low
732 calcination temperature (close to the crystallite size) to $d = d_{max} \sim 1000$ nm at high CO₂
733 partial pressure/high calcination temperature, which leads to an estimated surface area close
734 to a residual surface area of ~ 1 m²/g as measured experimentally. Under the conditions
735 of our experiments, our results are consistent with a sintering mechanism based on CaO
736 grain growth by lattice diffusion and enhanced by the increase of surface energy due to CO₂
737 adsorption on the CaO grains. The evolution of grain size with the calcination time (t_s)
738 may be adjusted for short sintering times by the simple empirical law: $d \sim d_0(1 + k_s t_s)$ with
739 $k_s \simeq 10^9 \times P^{0.5} \exp(-E_s/RT)$ min⁻¹ (P in Pa), $E_s \simeq 250$ kJ/mol (activation energy for
740 sintering), and $d_0 \simeq 15$ nm.

741 The reactivity of CaO produced by calcination in our tests scales proportionally to the
742 CaO surface area and therefore is severely hindered by the presence of CO₂ at high partial
743 pressure. Our in-situ XRD analysis shows that the CaO surface does not grow preferentially
744 along poorly reactive crystallographic planes as suggested in recent theoretical works even
745 though further analysis must be carried out to check this observation in the case of CaO
746 resulting from multiple carbonation/calcination cycles. Thus, CaO reactivity approaches a
747 residual value, which is determined by the residual surface area. Aggregation of nanocrystals
748 during the transformation would be hindered by the presence of thermally stable inert

749 nanograins, which would prevent sintering and therefore the loss of CaO carbonation reac-
750 tivity as seen for $CaO \cdot MgO$ derived from dolomite calcination and for synthetic CaO-based
751 composites. Moreover, $CaCO_3$ decarbonation in these composites would be accelerated as
752 observed experimentally [30] since crystal impurities promote diffusion of desorbed CO_2 and
753 metastable CaO* therefore enhancing the desorption/structural transformation step at CO_2
754 partial pressures close to equilibrium.

755 VIII. ACKNOWLEDGEMENTS

756 This work was supported by the Andalusian Regional Government Junta de Andalucia
757 (contracts FQM-5735 and TEP-7858), Spanish Government Agency Ministerio de Economia
758 y Competitividad and FEDER funds (contracts FIS2011-25161 and CTQ2011-27626). One
759 of the authors (PESJ) is supported by the Juan de la Cierva program of the Spanish Minis-
760 terio de Economia y Competitividad. We gratefully acknowledge the Microscopy, Functional
761 Characterization and X-ray services of the Innovation, Technology and Research Center of
762 the University of Seville (CITIUS). The help from Drs. Santiago Medina, Javier Quispe and
763 Francisco M. Varela (CITIUS) is specially recognized. Collaboration from Professor Joaquin
764 Bastida, who kindly provided us with the LaB_6 certified sample, is warmly appreciated.

765 IX. REFERENCES

-
- 766 [1] C. Rrodriguez-Navarro, E. Ruiz-Agudo, A. Luque, A. B. Navarro, and M. Ortega-Huertas,
767 “Thermal decomposition of calcite: Mechanisms of formation and textural evolution of cao
768 nanocrystals,” *American Mineralogist*, vol. 94, p. 578–593, 2009.

- 769 [2] J. Blamey, E. J. Anthony, J. Wang, and P. S. Fennell, “The calcium looping cycle for large-
770 scale CO₂ capture,” *Prog. Energ. Combust. Sci.*, vol. 36, no. 2, pp. 260–279, 2010.
- 771 [3] M. C. Romano, “Modeling the carbonator of a Ca-looping process for CO₂ capture from power
772 plant flue gas,” *Chemical Engineering Science*, vol. 69, pp. 257 – 269, 2012.
- 773 [4] B. Arias, M. Diego, J. Abanades, M. Lorenzo, L. Diaz, D. Martinez, J. Alvarez, and
774 A. Sanchez-Biezma, “Demonstration of steady state CO₂ capture in a 1.7 MWth calcium
775 looping pilot,” *International Journal of Greenhouse Gas Control*, vol. 18, pp. 237–245, 2013.
- 776 [5] S. E. Edwards and V. Materic, “Calcium looping in solar power generation plants,” *Solar
777 Energy*, vol. 86, no. 9, pp. 2494 – 2503, 2012.
- 778 [6] G. Flamant, D. Hernandez, C. Bonet, and J.-P. Traverse, “Experimental aspects of the ther-
779 mochemical conversion of solar energy; decarbonation of caco₃,” *Solar Energy*, vol. 24, no. 4,
780 pp. 385 – 395, 1980.
- 781 [7] J. M. Valverde, P. E. Sanchez-Jimenez, and L. A. Perez-Maqueda, “Calcium-looping for post-
782 combustion CO₂ capture. on the adverse effect of sorbent regeneration under CO₂,” *Applied
783 Energy*, vol. 126, pp. 161–171, 2014.
- 784 [8] J. M. Valverde, P. E. Sanchez-Jimenez, and L. A. Perez-Maqueda, “On the relevant influence
785 of limestone crystallinity on CO₂ capture in the ca-looping technology at realistic calcination
786 conditions,” *Environmental Science & Technology*, vol. 48, no. 16, pp. 9882–9889, 2014.
- 787 [9] E. P. Hyatt, I. B. Cutler, and M. E. Wadsworth, “Calcium carbonate decomposition in carbon
788 dioxide atmosphere,” *Journal of the American Ceramic Society*, vol. 41, no. 2, pp. 70–74, 1958.
- 789 [10] D. Beruto, L. Barco, and A. W. Searcy, “CO₂-catalyzed surface area and porosity changes in
790 high-surface-area CaO aggregates,” *Journal of the American Ceramic Society*, vol. 67, no. 7,
791 pp. 512–516, 1984.

- 792 [11] E. L. Fuller and T. R. Yoos, "Surface properties of limestones and their activation products,"
793 *Langmuir*, vol. 3, no. 5, pp. 753–760, 1987.
- 794 [12] J. M. Criado, M. Macias, and A. Macias-Machin, "Analysis of the system CaO-CO₂-H₂O for
795 storage of solar thermal energy," *Solar Energy*, vol. 49, pp. 83–86, 1992.
- 796 [13] J. M. Criado, M. Gonzalez, J. Malek, and A. Ortega, "The effect of the CO₂ pressure on the
797 thermal decomposition kinetics of calcium carbonate," *Thermochimica Acta*, vol. 254, pp. 121
798 – 127, 1995.
- 799 [14] J. Khinast, G. Krammer, C. Brunner, and G. Staudinger, "Decomposition of limestone: The
800 influence of CO₂ and particle size on the reaction rate," *Chemical Engineering Science*, vol. 51,
801 no. 4, pp. 623–634, 1996.
- 802 [15] D. Dollimore, P. Tong, and K. S. Alexander, "The kinetic interpretation of the decomposition
803 of calcium carbonate by use of relationships other than the arrhenius equation," *Thermochimica
804 Acta*, vol. 282–283, pp. 13 – 27, 1996.
- 805 [16] N. Koga and J. M. Criado, "The influence of mass transfer phenomena on the kinetic analysis
806 for the thermal decomposition of calcium carbonate by constant rate thermal analysis (CRTA)
807 under vacuum," *Int. J. Chem. Kinet.*, vol. 30, pp. 737–744, 1998.
- 808 [17] F. Garcia-Labiano, A. Abad, L. de Diego, P. Gayan, and J. Adanez, "Calcination of calcium-
809 based sorbents at pressure in a broad range of CO₂ concentrations," *Chemical Engineering
810 Science*, vol. 57, no. 13, pp. 2381 – 2393, 2002.
- 811 [18] D. Beruto, A. W. Searcy, and M. G. Kim, "Microstructure, kinetic, structure, thermodynamic
812 analysis for calcite decomposition: free-surface and powder bed experiments," *Thermochimica
813 Acta*, vol. 424, no. 1–2, pp. 99 – 109, 2004.

- 814 [19] P. Michele, F. Loic, and S. Michel, "From the drawbacks of the arrhenius-f(α) rate equation
815 towards a more general formalism and new models for the kinetic analysis of solid - gas
816 reactions," *Thermochimica Acta*, vol. 525, no. 1–2, pp. 93 – 102, 2011.
- 817 [20] I. Barin, *Thermochemical data of pure substances*. Weinheim: VCH., 1989.
- 818 [21] B. Stanmore and P. Gilot, "Review - calcination and carbonation of limestone during thermal
819 cycling for CO₂ sequestration," *Fuel Processing Technology*, vol. 86, no. 16, pp. 1707 – 1743,
820 2005.
- 821 [22] A. K. Galwey and M. E. Brown, "Application of the arrhenius equation to solid state kinetics:
822 can this be justified?," *Thermochimica Acta*, vol. 386, no. 1, pp. 91 – 98, 2002.
- 823 [23] A. Khawam and D. R. Flanagan, "Solid-state kinetic models: Basics and mathematical fun-
824 damentals," *The Journal of Physical Chemistry B*, vol. 110, no. 35, pp. 17315 – 17328, 2006.
- 825 [24] D. Beruto and A. W. Searcy, "Use of the langmuir method for kinetic studies of decomposition
826 reactions: calcite (caco₃)," *J. Chem. Soc., Faraday Trans. 1*, vol. 70, pp. 2145–2153, 1974.
- 827 [25] C. N. R. Rao, S. R. Yoganarasimhan, and M. P. Lewis, "Exothermic reactions due to annealing
828 of defects in oxide lattices: Study of the decomposition of carbonates," *Canadian Journal of
829 Chemistry*, vol. 38, no. 12, pp. 2359–2362, 1960.
- 830 [26] N. Rodriguez, M. Alonso, G. Grasa, and J. C. Abanades, "Heat requirements in a calciner
831 of CaCO₃ integrated in a CO₂ capture system using CaO," *Chemical Engineering Journal*,
832 vol. 138, no. 1–3, pp. 148–154, 2008.
- 833 [27] L. M. Romeo, Y. Lara, P. Lisbona, and J. M. Escosa, "Optimizing make-up flow in a CO₂
834 capture system using CaO," *Chemical Engineering Journal*, vol. 147, no. 2-3, pp. 252 – 258,
835 2009.

- 836 [28] A. Martinez, Y. Lara, P. Lisbona, and L. M. Romeo, "Operation of a cyclonic preheater
837 in the Ca-looping for CO₂ capture," *Environmental Science & Technology*, vol. 47, no. 19,
838 pp. 11335–11341, 2013.
- 839 [29] I. Martinez, G. Grasa, R. Murillo, B. Arias, and J. Abanades, "Modelling the continuous
840 calcination of CaCO₃ in a Ca-looping system," *Chemical Engineering Journal*, vol. 215–216,
841 pp. 174–181, 2013.
- 842 [30] J. Valverde, P. Sanchez-Jimenez, and L. Perez-Maqueda, "Ca-looping for postcombustion
843 {CO₂} capture: A comparative analysis on the performances of dolomite and limestone,"
844 *Applied Energy*, vol. 138, no. 0, pp. 202 – 215, 2015.
- 845 [31] R. Besson, M. R. Vargas, and L. Favregeon, "CO₂ adsorption on calcium oxide: An atomic-
846 scale simulation study," *Surface Science*, vol. 606, no. 3–4, pp. 490 – 495, 2012.
- 847 [32] R. Besson and L. Favregeon, "Atomic - scale study of calcite nucleation in calcium oxide,"
848 *The Journal of Physical Chemistry C*, vol. 117, no. 17, pp. 8813 – 8821, 2013.
- 849 [33] J. P. Allen, A. Marmier, and S. C. Parker, "Atomistic simulation of surface selectivity on
850 carbonate formation at calcium and magnesium oxide surfaces," *The Journal of Physical
851 Chemistry C*, vol. 116, no. 24, pp. 13240 – 13251, 2012.
- 852 [34] M. Alonso, Y. Criado, J. Abanades, and G. Grasa, "Undesired effects in the determination of
853 CO₂ carrying capacities of CaO during TG testing," *Fuel*, vol. 127, pp. 52–61, 2014.
- 854 [35] G. Grasa, R. Murillo, M. Alonso, and J. C. Abanades, "Application of the random pore model
855 to the carbonation cyclic reaction," *AIChE J.*, vol. 55, no. 5, pp. 1246–1255, 2009.
- 856 [36] M. E. Brown, "The prout-tompkins rate equation in solid-state kinetics," *Thermochimica
857 Acta*, vol. 300, no. 1 - 2, pp. 93 – 106, 1997.

- 858 [37] S. Grazulis, A. Daskevicius, A. Merkys, D. Chateigner, L. Lutterotti, M. Quiros, N. R. Sere-
859 bryanaya, P. Moeck, R. T. Downs, and A. Le Bail, “Crystallography open database (COD):
860 an open-access collection of crystal structures and platform for world-wide collaboration,”
861 *Nucleic Acids Research*, vol. 40, no. D1, pp. D420–D427, 2012.
- 862 [38] K. M. Towe, “Ultrastructure of calcite decomposition in vacuo,” *Nature*, vol. 274, pp. 239 –
863 240, 1978.
- 864 [39] S. Dash, M. Kamruddin, P. Ajikumar, A. Tyagi, and B. Raj, “Nanocrystalline and metastable
865 phase formation in vacuum thermal decomposition of calcium carbonate,” *Thermochimica*
866 *Acta*, vol. 363, no. 1-2, pp. 129–135, 2000.
- 867 [40] N. Fatemi, R. Whitehead, D. Price, and D. Dollimore, “Some comments on the use of
868 avrami-erofeev expressions and solid state decomposition rate constants,” *Thermochimica*
869 *Acta*, vol. 104, no. 0, pp. 93 – 100, 1986.
- 870 [41] P. E. Sanchez-Jimenez, A. Perejon, J. M. Criado, M. J. Dianez, and L. A. Perez-Maqueda,
871 “Kinetic model for thermal dehydrochlorination of poly(vinyl chloride),” *Polymer*, vol. 51,
872 no. 17, pp. 3998 – 4007, 2010.
- 873 [42] P. Sun, J. R. Grace, C. J. Lim, and E. J. Anthony, “Determination of intrinsic rate constants
874 of the CaO - CO₂ reaction,” *Chemical Engineering Science*, vol. 63, no. 1, pp. 47 – 56, 2008.
- 875 [43] A. Negi and S. Anand, *A Textbook of Physical Chemistry*. Wiley Eastern, 1985.
- 876 [44] M. Pijolat and M. Soustelle, “Experimental tests to validate the rate-limiting step assumption
877 used in the kinetic analysis of solid–state reactions,” *Thermochimica Acta*, vol. 478, no. 1–2,
878 pp. 34 – 40, 2008.
- 879 [45] A. M. Kierzkowska, R. Pacciani, and C. R. Müller, “CaO-based CO₂ sorbents: From funda-
880 mentals to the development of new, highly effective materials,” *ChemSusChem*, vol. 6, no. 7,

- 881 pp. 1130–1148, 2013.
- 882 [46] A. W. Searcy and D. Beruto, “Kinetics of endothermic decomposition reactions. i. steady-state
883 chemical steps,” *The Journal of Physical Chemistry*, vol. 80, no. 4, pp. 425–429, 1976.
- 884 [47] D. Beruto, A. W. Searcy, and M. G. Kim, “Calcium oxides of high reactivity,” *Nature*,
885 vol. 5574, pp. 221 – 222, 1976.
- 886 [48] J. Rouquerol, “Critical examination of several problems typically found in the kinetic study of
887 thermal decomposition under vacuum,” *Journal of thermal analysis*, vol. 5, no. 2–3, pp. 203–
888 216, 1973.
- 889 [49] H.-Y. Xie and D. Geldart, “Fluidization of FCC powders in the bubble-free regime: effect
890 types of gases and temperature,” *Powder Technol.*, vol. 82, pp. 269 – 277, 1995.
- 891 [50] R. H. Borgwardt, “Sintering of nascent calcium oxide,” *Chem. Eng. Sci.*, vol. 44, no. 1, pp. 53–
892 60, 1989.
- 893 [51] R. H. Borgwardt, “Calcium oxide sintering in atmospheres containing water and carbon diox-
894 ide,” *Industrial & Engineering Chemistry Research*, vol. 28, no. 4, pp. 493 – 500, 1989.
- 895 [52] J. Valverde, J. M. P. Ebri, and M. A. S. Quintanilla, “Acoustic streaming enhances the mul-
896 ticyclic CO₂ capture of natural limestone at Ca-looping conditions,” *Environmental Science*
897 *& Technology*, vol. 47, no. 16, p. 9538–9544, 2013.
- 898 [53] R. M. German and Z. A. Munir, “Surface area reduction during isothermal sintering,” *Journal*
899 *of the American Ceramic Society*, vol. 59, no. 9 - 10, p. 379–383, 1976.
- 900 [54] D. Dollimore, “Thermodynamic, kinetic and surface texture factors in the production of active
901 solids by thermal decomposition,” *Journal of thermal analysis*, vol. 38, no. 1-2, pp. 111 – 130,
902 1992.

- 903 [55] C. R. Milne, G. D. Silcox, D. W. Pershing, and D. A. Kirchgessner, “Calcination and sintering
904 models for application to high-temperature, short-time sulfation of calcium-based sorbents,”
905 *Industrial & Engineering Chemistry Research*, vol. 29, no. 2, pp. 139–149, 1990.
- 906 [56] A. B. Fuertes, D. Alvarez, F. Rubiera, J. J. Pis, and G. Marban, “Surface area and pore size
907 changes during sintering of calcium oxide particles,” *Chemical Engineering Communications*,
908 vol. 109, no. 1, pp. 73 – 88, 1991.
- 909 [57] C. H. Bartholomew, “Sintering kinetics of supported metals: new perspectives from a unifying
910 GPLE treatment,” *Applied Catalysis A: General*, vol. 107, no. 1, pp. 1 – 57, 1993.
- 911 [58] G. Silcox, J. Kramlich, and D. Pershing, “A mathematical model for the flash calcination of
912 dispersed CaCO_3 and $\text{Ca}(\text{OH})_2$ particles,” *Ind. Eng. Chem. Res.*, vol. 28, p. 155 – 160, 1989.
- 913 [59] G. S. Grasa and J. C. Abanades, “ CO_2 capture capacity of CaO in long series of carbona-
914 tion/calcination cycles,” *Ind. Eng. Chem. Res.*, vol. 45, no. 26, pp. 8846–8851, 2006.
- 915 [60] J. M. Valverde, P. E. Sanchez Jimenez, A. Perejon, and L. A. Perez-Maqueda, “ CO_2 multicyclic
916 capture of pretreated/doped CaO in the Ca – looping process. Theory and experiments,” *Phys.*
917 *Chem. Chem. Phys.*, vol. 15, pp. 11775 – 11793, 2013.
- 918 [61] J. Ewing, D. Beruto, and A. W. Searcy, “The nature of CaO produced by calcite powder
919 decomposition in vacuum and in CO_2 ,” *Journal of the American Ceramic Society*, vol. 62,
920 no. 11-12, pp. 580–584, 1979.
- 921 [62] S. Stendardo, L. Andersen, and C. Hecce, “Self-activation and effect of regeneration conditions
922 in CO_2 carbonate looping with CaO Ca_{12} Al_{14} O_{33} sorbent,” *Chemical Engineering Journal*,
923 vol. 220, pp. 383 – 394, 2013.
- 924 [63] R. Barker, “Reversibility of the reaction $\text{CaCO}_3 = \text{CaO} + \text{CO}_2$,” *J. Appl. Chem. Biotechnol.*,
925 vol. 23, pp. 733 – 742, 1973.

- 926 [64] S. K. Bhatia and D. D. Perlmutter, "Effect of the product layer on the kinetics of the CO₂-lime
927 reaction," *AIChE Journal*, vol. 29, no. 1, pp. 79–86, 1983.
- 928 [65] Z. Sun, S. Luo, P. Qi, and L.-S. Fan, "Ionic diffusion through calcite (CaCO₃) layer during
929 the reaction of cao and CO₂," *Chemical Engineering Science*, vol. 81, pp. 164 – 168, 2012.
- 930 [66] J. M. Valverde, "A model on the CaO multicyclic conversion in the Ca-looping process,"
931 *Chemical Engineering Journal*, vol. 228, pp. 1195–1206, 2013.
- 932 [67] D. Alvarez and J. C. Abanades, "Pore-size and shape effects on the recarbonation performance
933 of calcium oxide submitted to repeated calcination/recarbonation cycles," *Energy and Fuels*,
934 vol. 19, pp. 270–278, 2005.

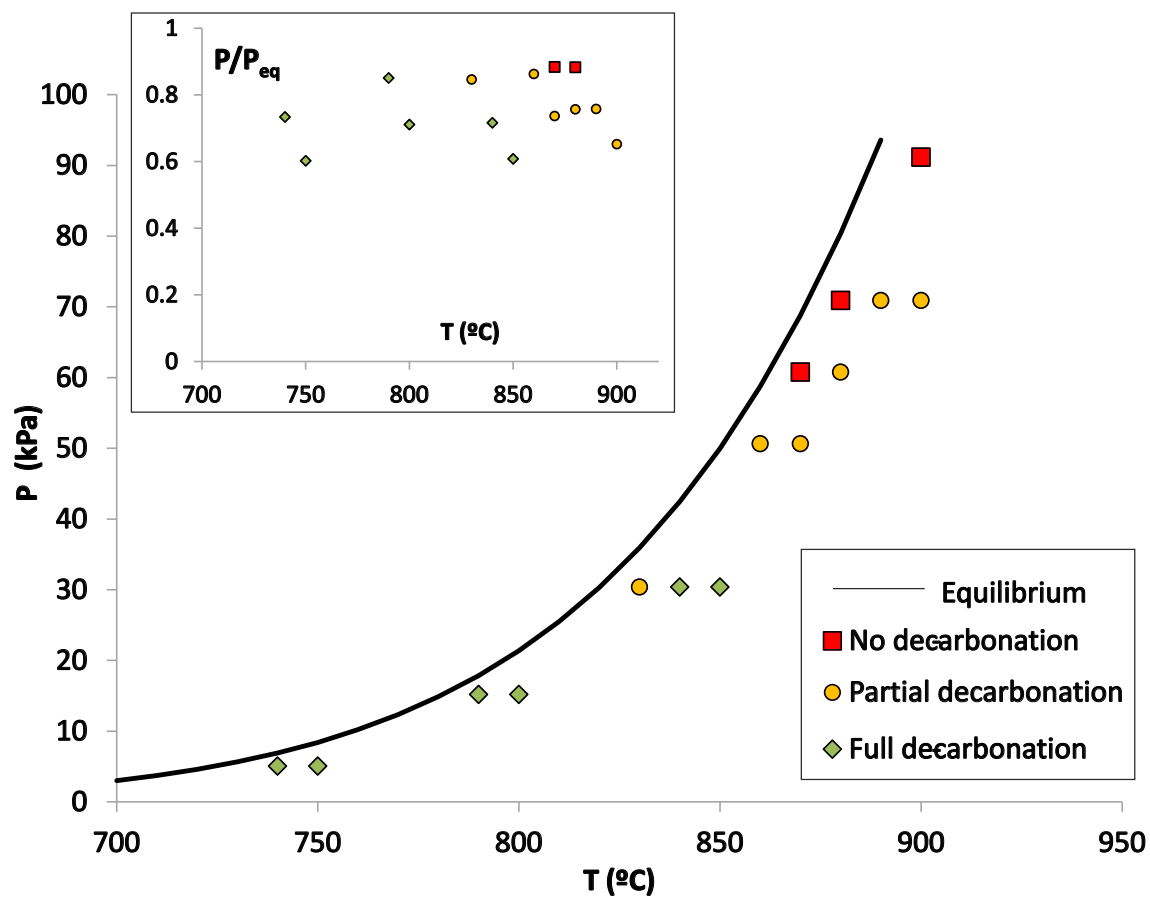


FIG. 1: CO₂ partial pressure P and temperature in the calcination tests carried out. It is indicated whether full decarbonation was achieved in the 1 h calcination period or partial decarbonation or no decarbonation at all (in-situ XRD analysis). The solid line represents the CO₂ equilibrium pressure as a function of temperature. The inset shows the ratio of CO₂ partial pressure to equilibrium pressure as a function of the calcination temperature.

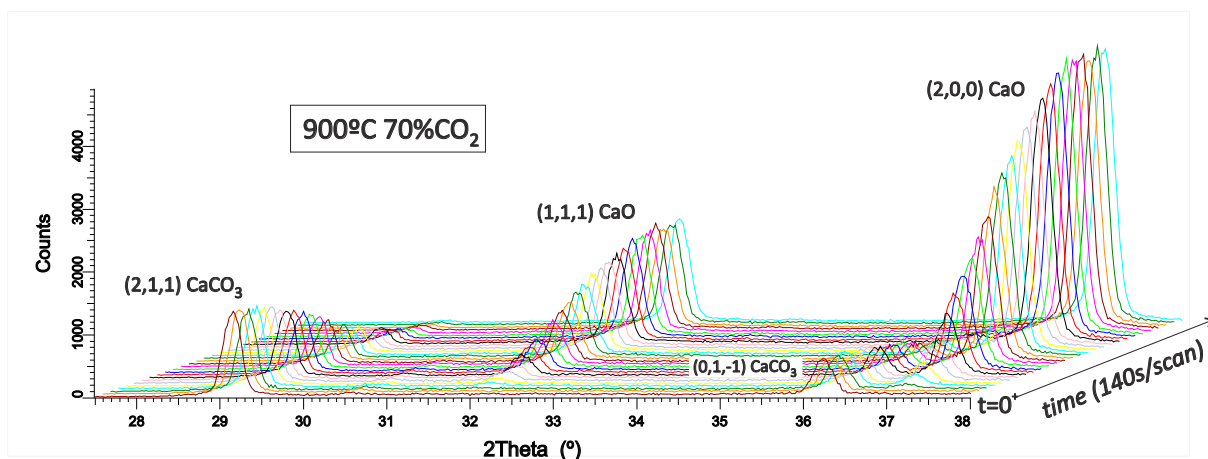


FIG. 2: Diffractograms obtained from in-situ XRD analysis during calcination at 900°C under 70% CO₂.

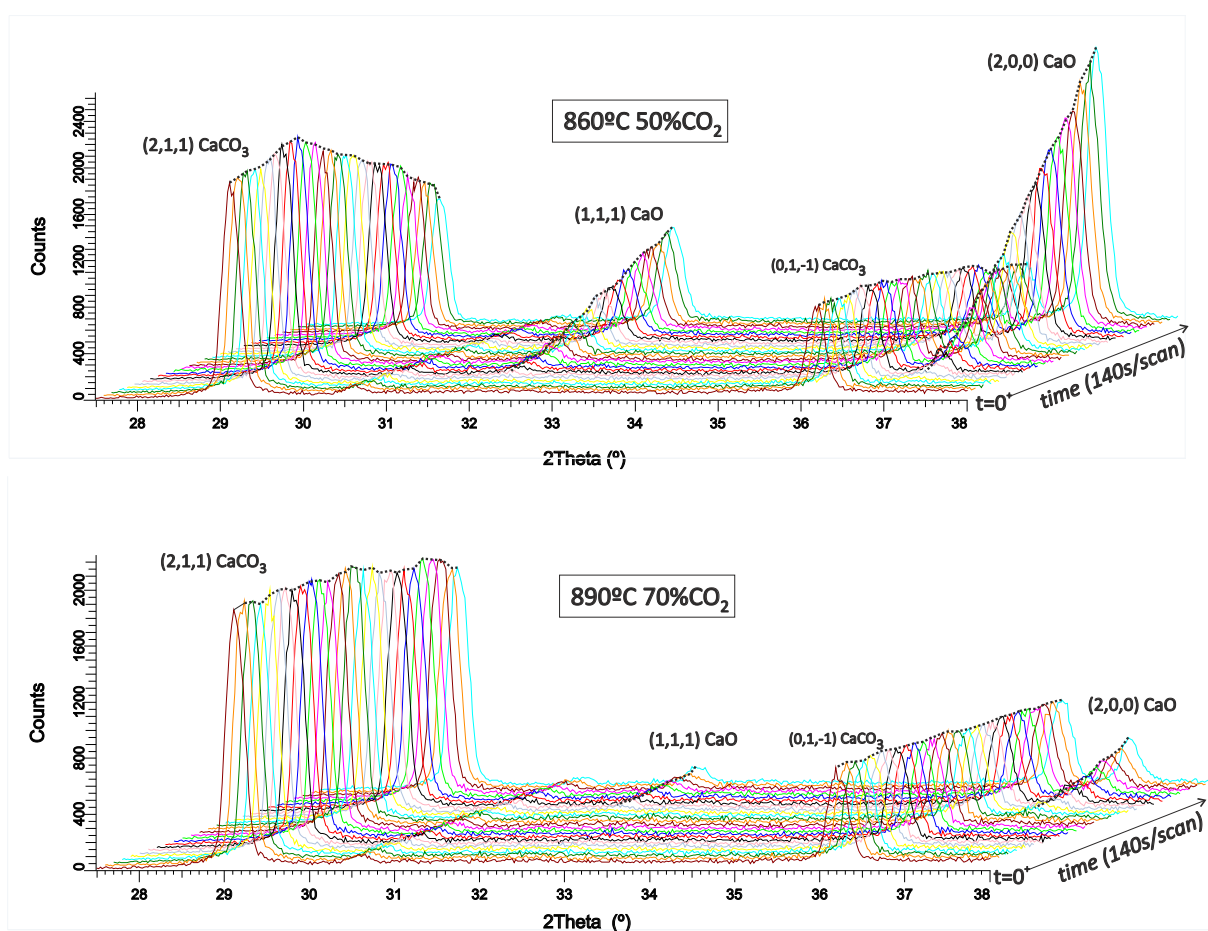


FIG. 3: Diffractograms obtained from in-situ XRD analysis during calcination at the conditions indicated.

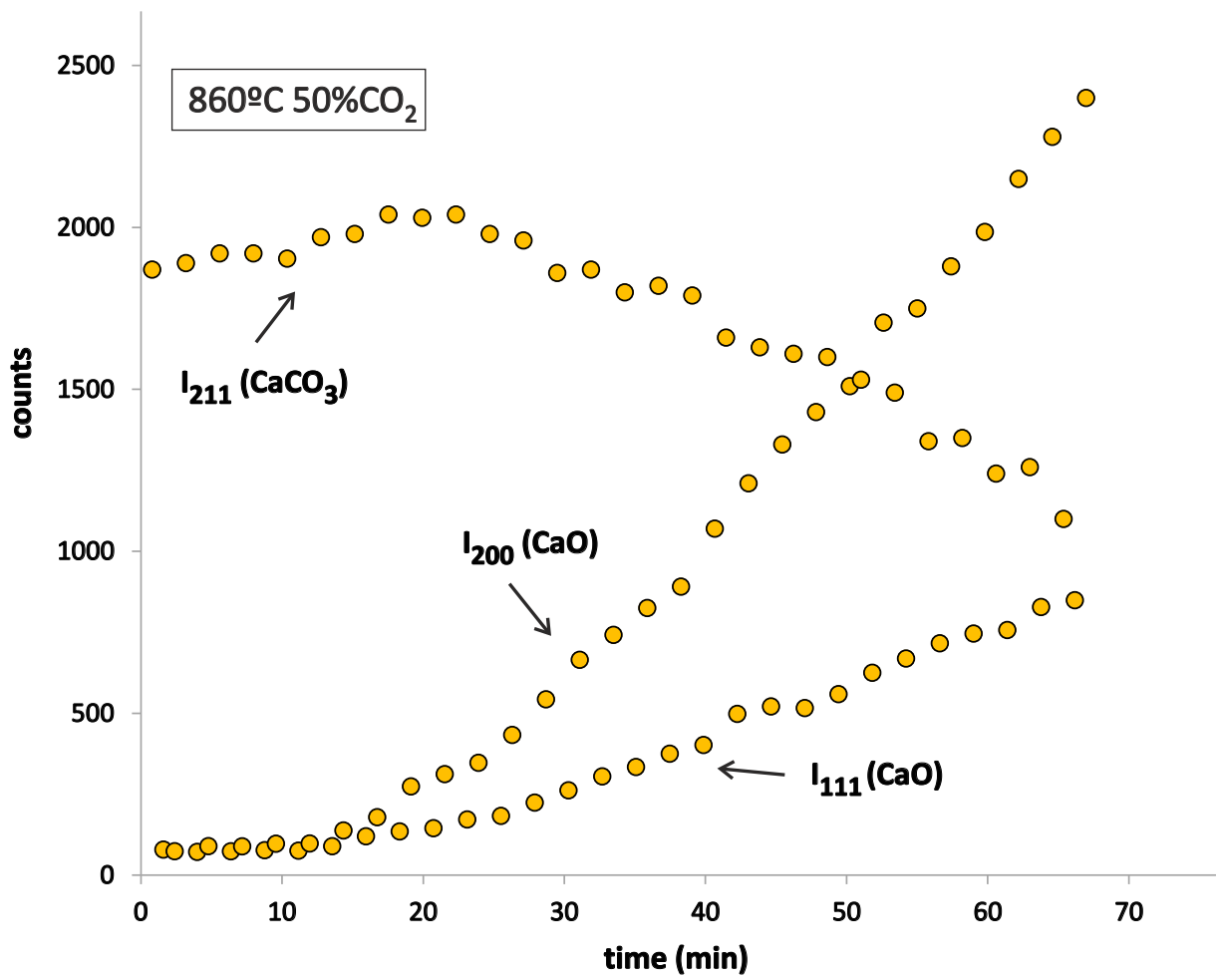


FIG. 4: Intensities at the indicated Bragg reflection peaks as a function of calcination time at 860°C/50%CO₂ obtained from in-situ XRD analysis.

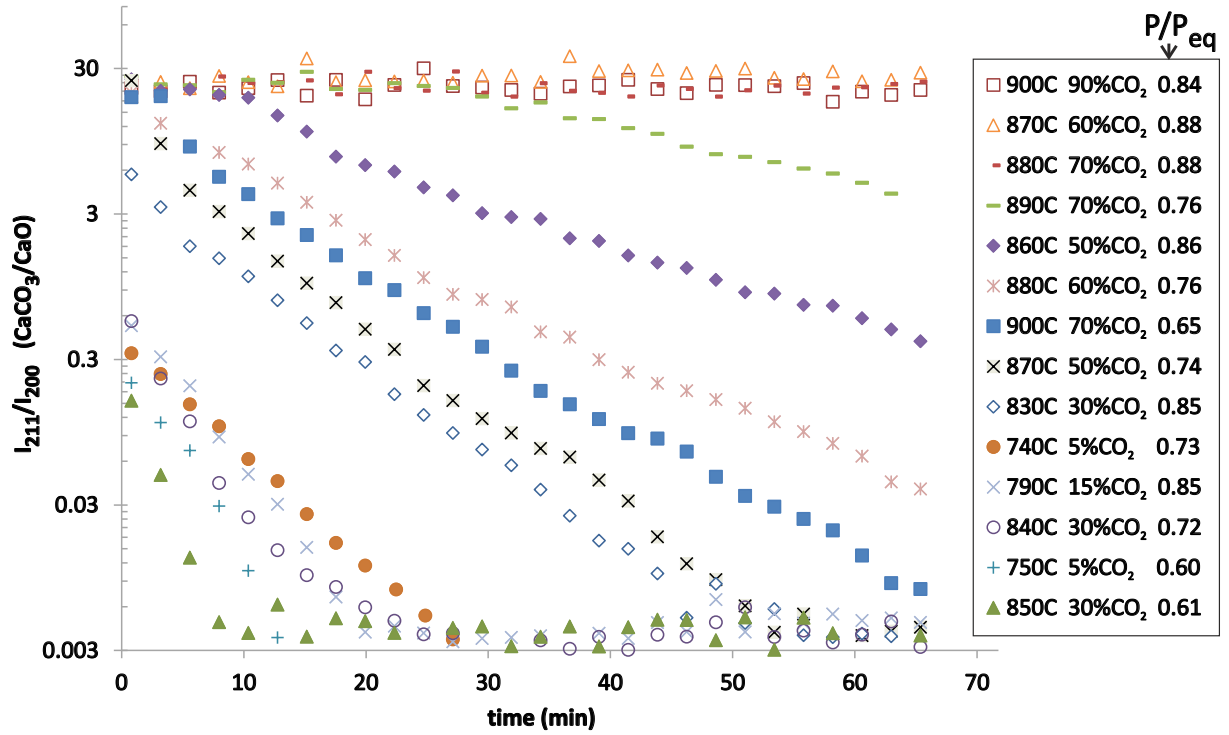


FIG. 5: Ratio of intensity at CaCO₃ (211) main reflection peak position ($2\theta \simeq 29.2^\circ$) to intensity at CaO (200) main peak position ($2\theta \simeq 37.1^\circ$) during calcination at diverse temperatures and CO₂ vol.% (as indicated) obtained during in-situ XRD analysis. Note the vertical log scale.

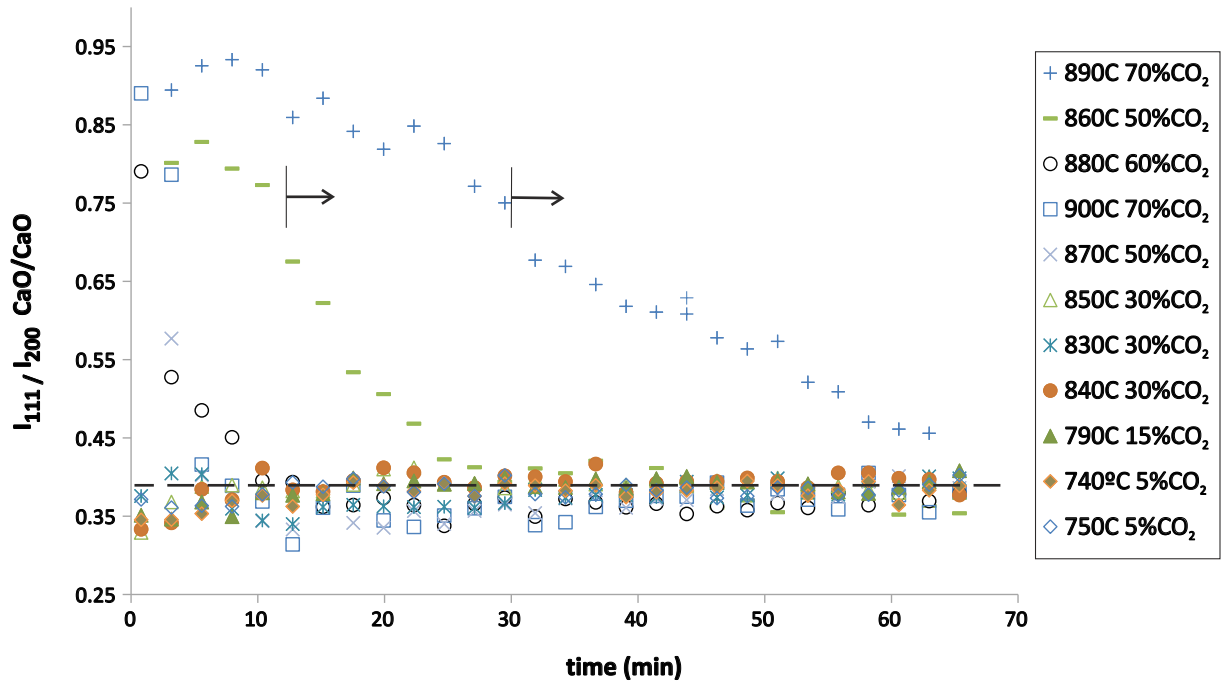


FIG. 6: Ratio of intensity at CaO (111) reflection peak position ($2\theta \simeq 32^\circ$) to intensity at CaO (200) peak position ($2\theta \simeq 37.1^\circ$) during calcination at diverse temperatures and CO_2 vol.% (as indicated) obtained by in-situ XRD analysis. The horizontal arrows indicate the initiation of decarbonation after an induction period as inferred from Fig. 5. The horizontal dashed line indicates the intensities ratio I_{111}/I_{200} given by the CaO (lime) reference pattern ($I_{111}/I_{200} = 0.389$) available from Crystallography Open Database (COD) [37].

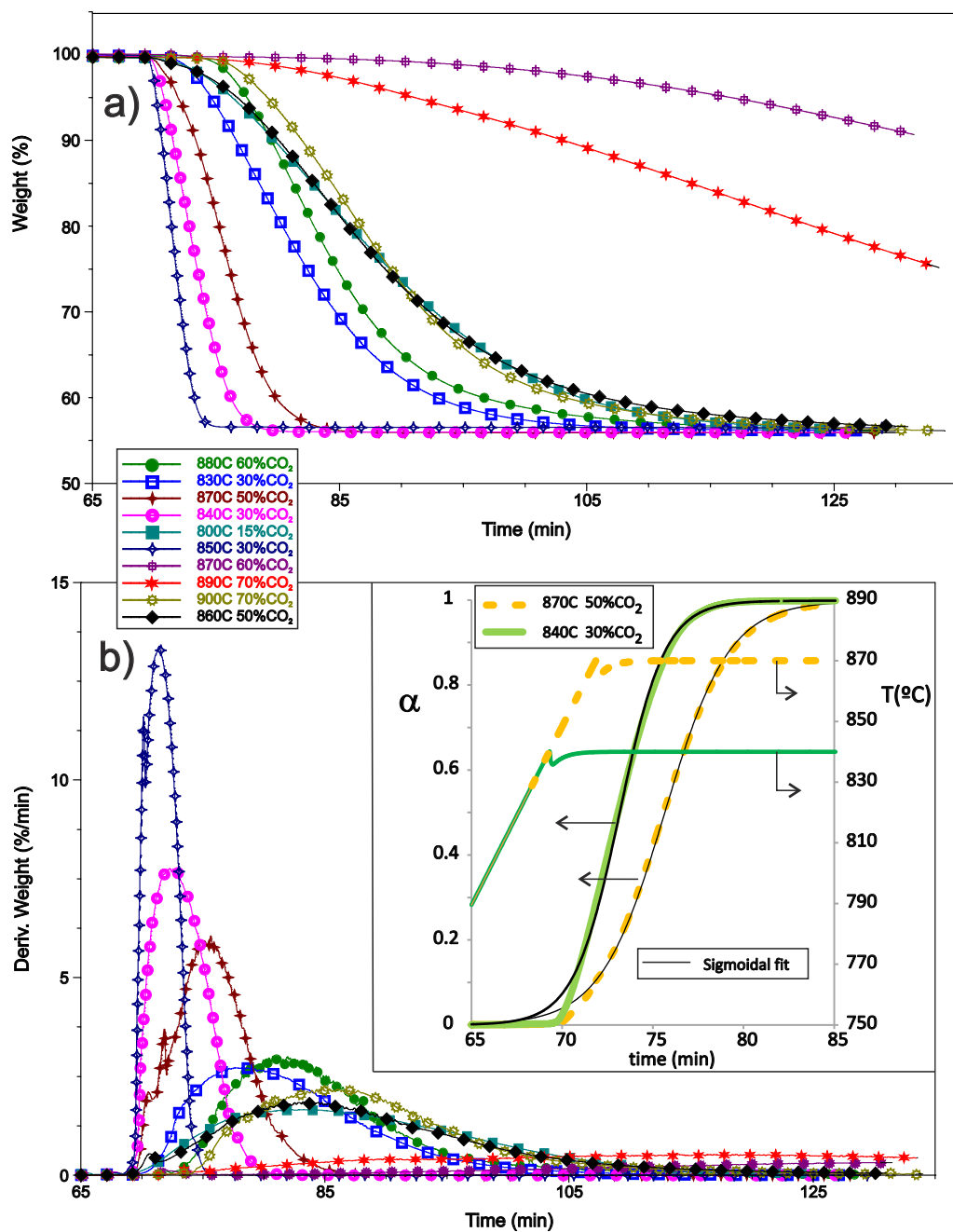


FIG. 7: Time evolution of sample weight (wt.%) (a) and weight % time derivative (b) measured in the TGA tests during calcination at diverse temperatures and CO₂ vol.% (as indicated). The inset of b) shows for two examples the time evolution of CaCO₃ conversion derived from the thermogram ($\alpha = (100/44)\Delta wt/wt_0$) and temperature in the tests. The solid lines represent best sigmoidal fit curves ($\alpha(t) \simeq 1/(1 + \exp(-\beta(t - t_0)))$)

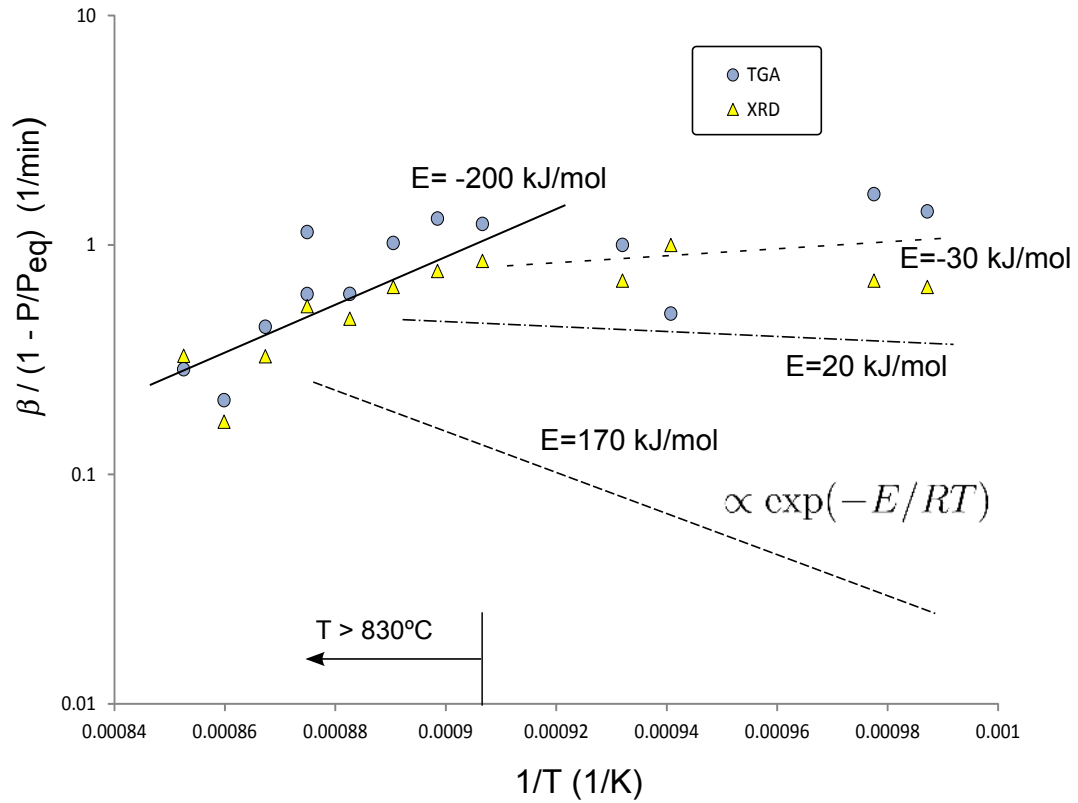


FIG. 8: Reaction rate divided by $(1 - P/P_{eq})$ as a function of $1/T(K)$ obtained from calcination tests by means of TGA and in-situ XRD analysis as indicated and predicted by the laws $r/(1 - P/P_{eq}) \propto \exp(-E/RT)$.

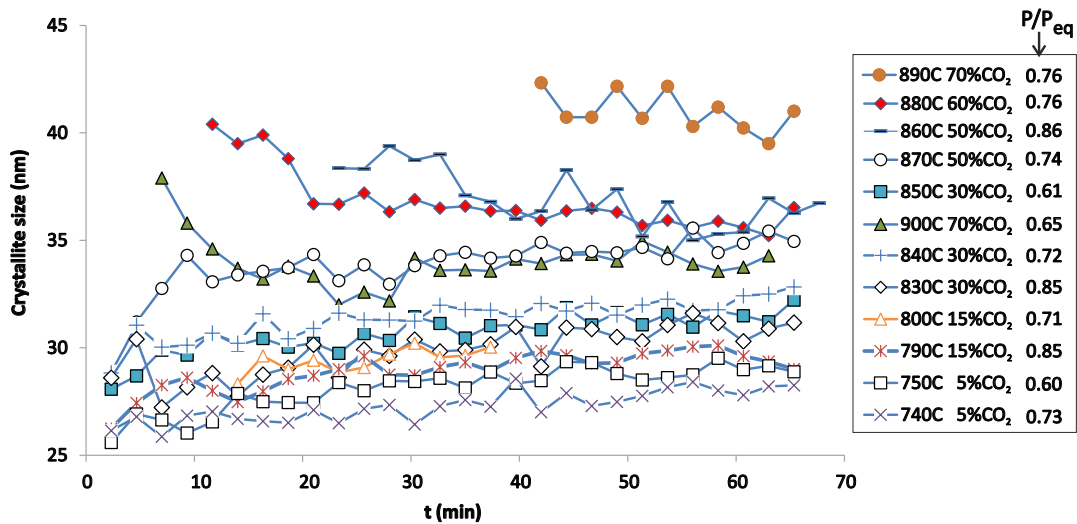


FIG. 9: CaO crystallite size (L_c) as a function of calcination time determined by CaO (200) peak broadening analysis from the in-situ XRD tests.

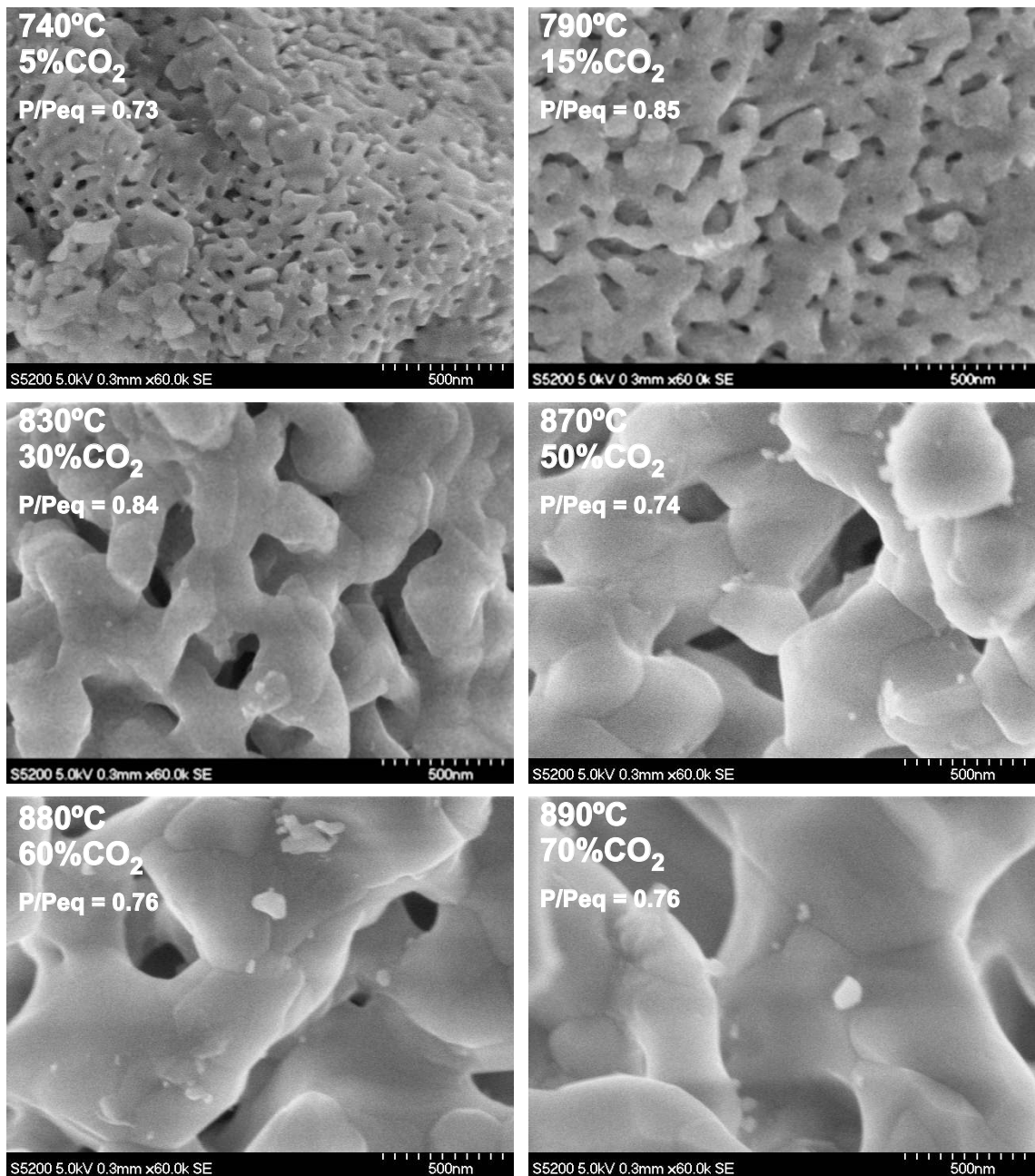


FIG. 10: Representative SEM images of samples calcined in the XRD chamber at diverse conditions of temperature and CO₂ concentration. Values of the ratio of CO₂ partial pressure to equilibrium partial pressure are indicated.

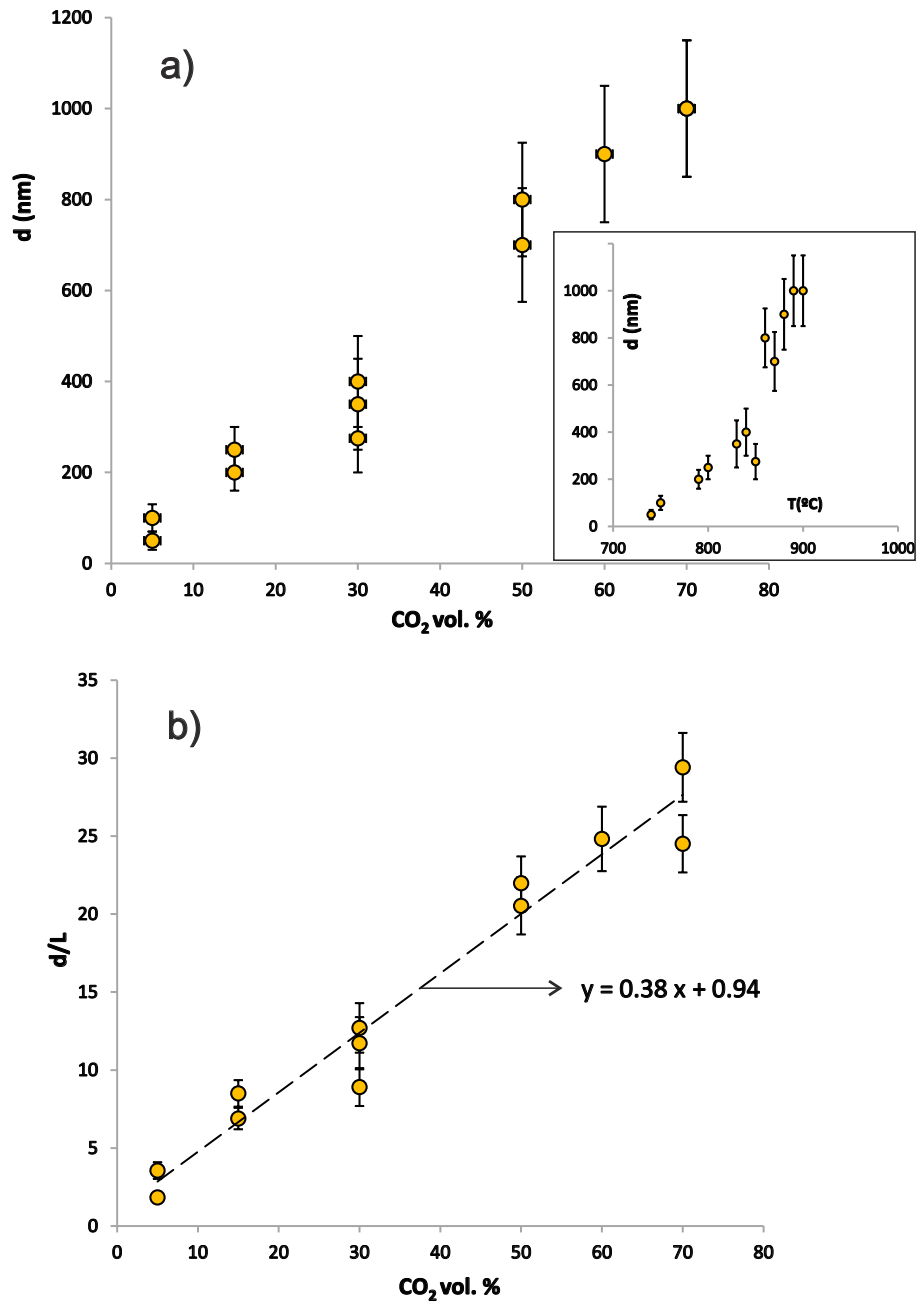


FIG. 11: a) CaO grain size d obtained from SEM images of samples calcined in the XRD chamber as a function of the CO_2 vol.% in the calcination atmosphere. The inset shows d versus the calcination temperature. b) Ratio of grain size to average crystallite size. The dashed line represents the best fit linear law ($d/L_c \simeq 1 + 0.4[\text{CO}_2 \text{ vol.}\%]$).

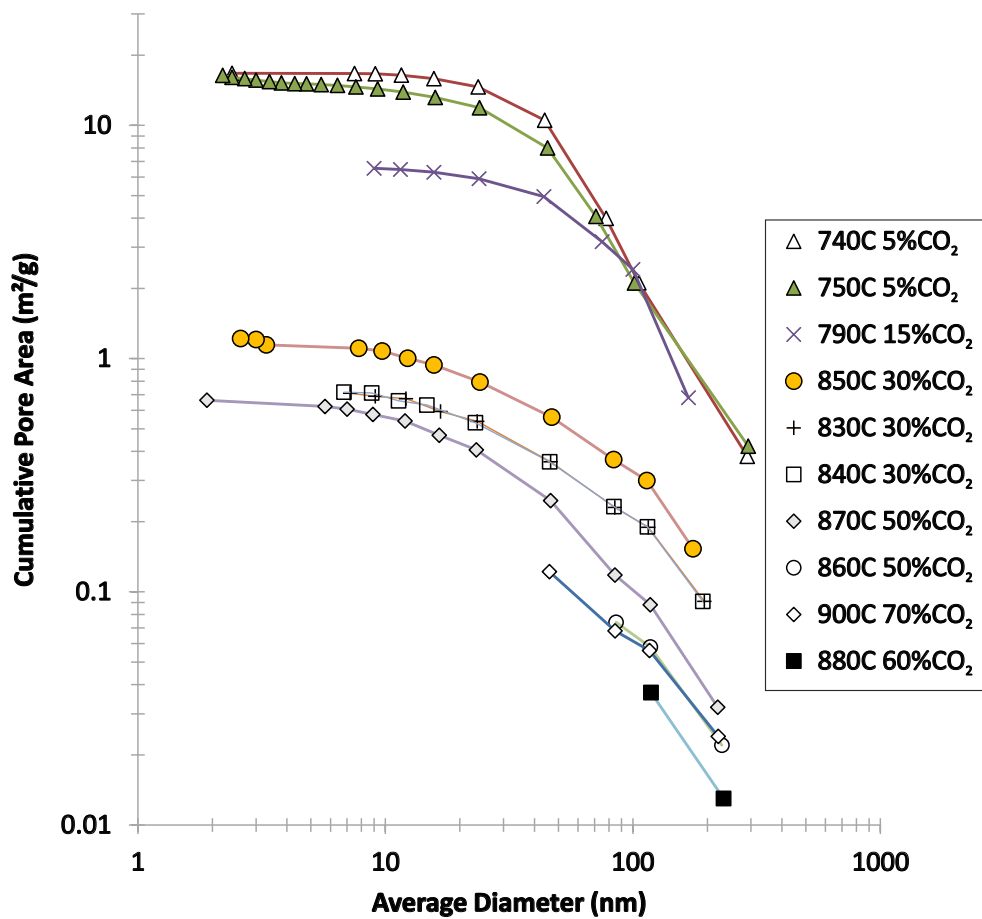


FIG. 12: Cumulative pore area distributions obtained by N₂ physisorption (77 K) analysis on the samples calcined in the XRD chamber.

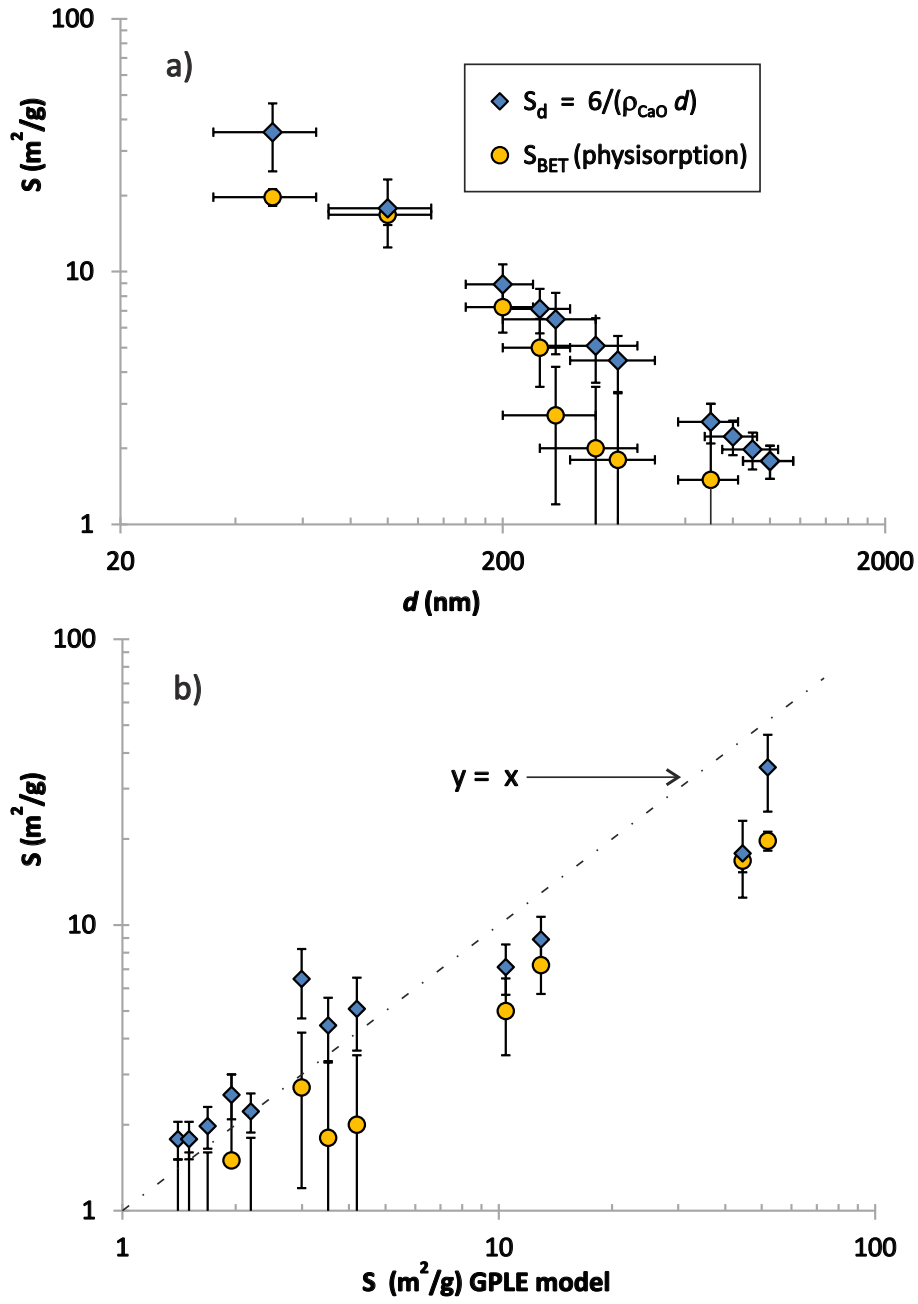


FIG. 13: a) Surface area of the samples calcined in the XRD chamber as a function of grain size d (obtained from SEM analysis, Fig. 11). Surface area values are shown as measured from N₂ physisorption analysis (S_{BET}) and estimated from grain size S_d . b) S_{BET} and S_d versus predicted values from equation Eq. 34 using $k = 10K_s$ (Eq. 32).

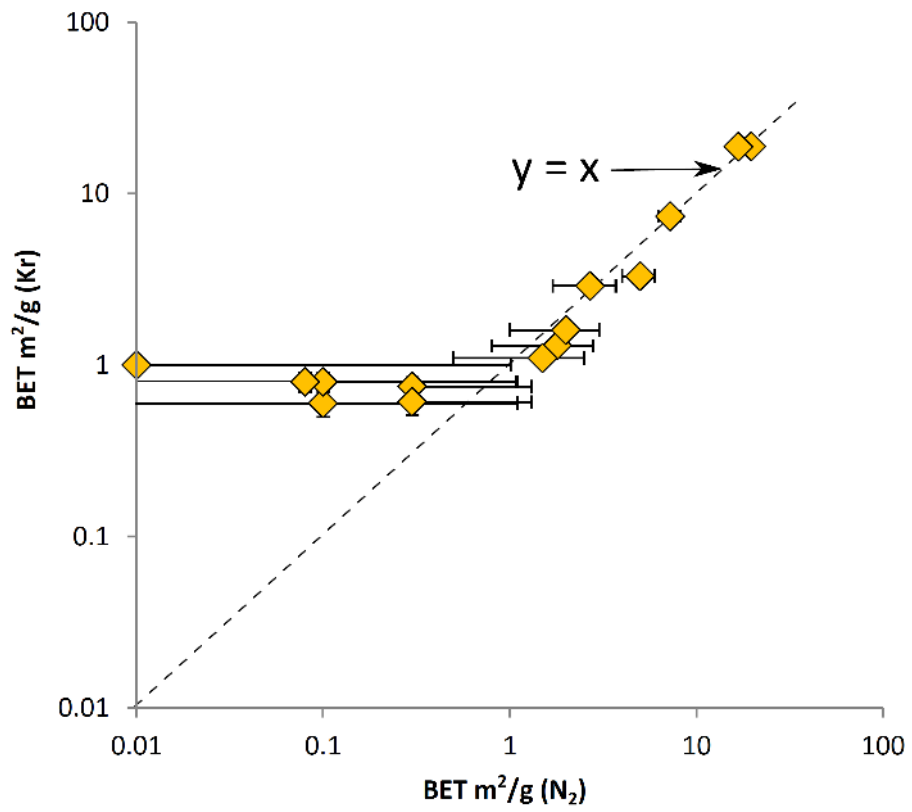


FIG. 14: BET surface area as measured from physisorption analysis using Kr (vertical axis) and N₂ (horizontal axis).

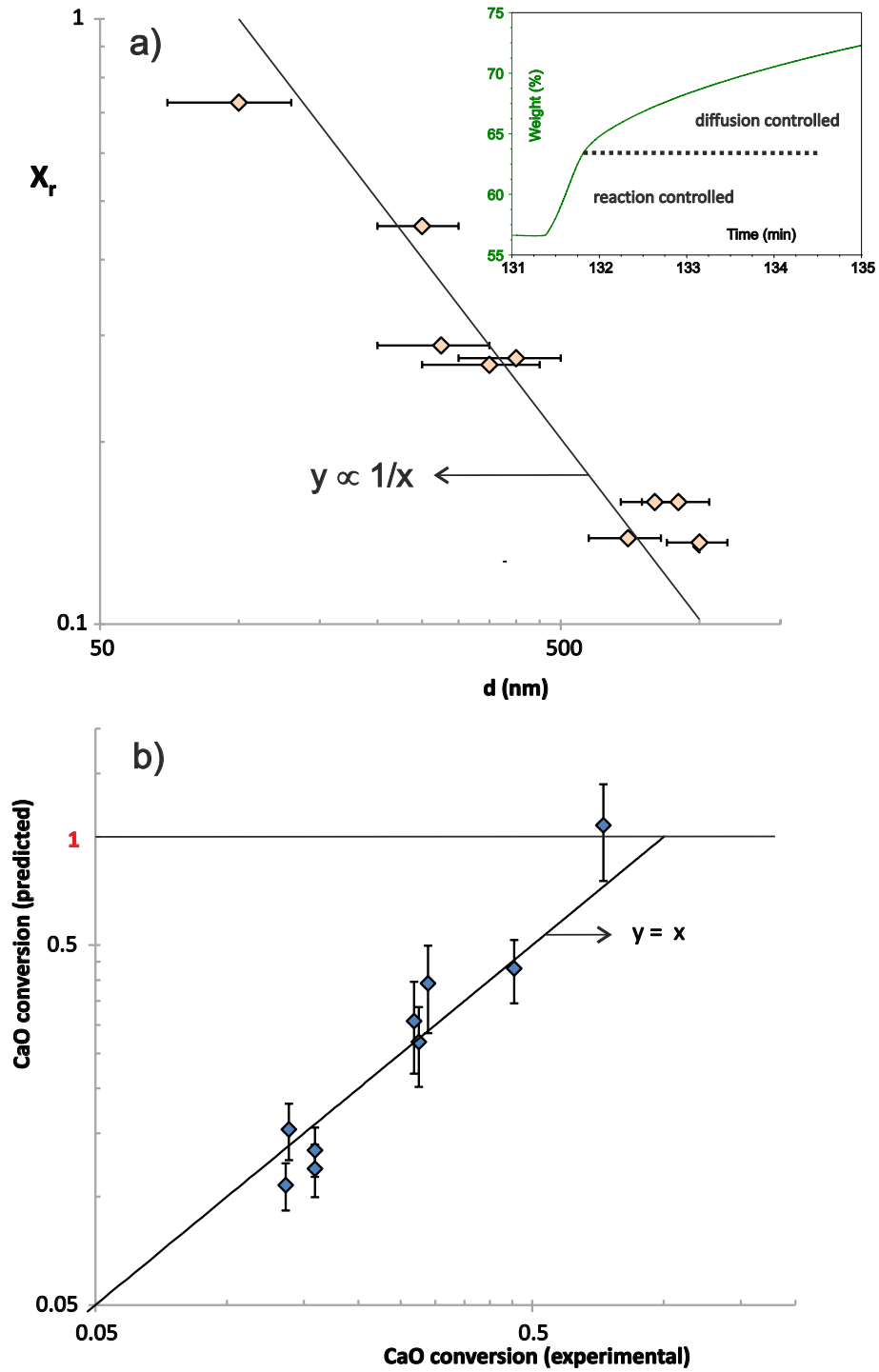


FIG. 15: a) CaO conversion in the reaction controlled phase measured in the TGA tests (at $650^{\circ}\text{C}/15\%\text{CO}_2$ just after calcination) as a function of grain size d derived from SEM analysis (Fig. 11). The inset shows the time evolution of sample wt% during carbonation of CaO derived from calcination in-situ ($860^{\circ}\text{C}/50\%\text{CO}_2$) illustrating the border between the reaction controlled and diffusion controlled carbonation phases. b) CaO conversion in the reaction controlled phase measured versus predicted from Eq. 35 using the surface area estimated from the grain size S_d and $h = 40$ nm.